

A random-jet-stirred turbulence tank

EVAN A. VARIANO[†] AND EDWIN A. COWEN

DeFrees Hydraulics Laboratory, School of Civil & Environmental Engineering, Cornell University,
Ithaca, NY 14853, USA

(Received 15 September 2006 and in revised form 14 January 2008)

We report measurements of the flow above a planar array of synthetic jets, firing upwards in a spatiotemporally random pattern to create turbulence at an air–water interface. The flow generated by this randomly actuated synthetic jet array (RASJA) is turbulent, with a large Reynolds number and a weak secondary (mean) flow. The turbulence is homogeneous over a large region and has similar isotropy characteristics to those of grid turbulence. These properties make the RASJA an ideal facility for studying the behaviour of turbulence at boundaries, which we do by measuring one-point statistics approaching the air–water interface (via particle image velocimetry). We explore the effects of different spatiotemporally random driving patterns, highlighting design conditions relevant to all randomly forced facilities. We find that the number of jets firing at a given instant, and the distribution of the duration for which each jet fires, greatly affect the resulting flow. We identify and study the driving pattern that is optimal given our tank geometry. In this optimal configuration, the flow is statistically highly repeatable and rapidly reaches steady state. With increasing distance from the jets, there is a jet merging region followed by a planar homogeneous region with a power-law decay of turbulent kinetic energy. In this homogeneous region, we find a Reynolds number of 314 based on the Taylor microscale. We measure all components of mean flow velocity to be less than 10% of the turbulent velocity fluctuation magnitude. The tank width includes roughly 10 integral length scales, and because wall effects persist for one to two integral length scales, there is sizable core region in which turbulent flow is unaffected by the walls. We determine the dissipation rate of turbulent kinetic energy via three methods, the most robust using the velocity structure function. Having a precise value of dissipation and low mean flow allows us to measure the empirical constant in an existing model of the Eulerian velocity power spectrum. This model provides a method for determining the dissipation rate from velocity time series recorded at a single point, even when Taylor’s frozen turbulence hypothesis does not hold. Because the jet array offers a high degree of flow control, we can quantify the effects of the mean flow in stirred tanks by intentionally forcing a mean flow and varying its strength. We demonstrate this technique with measurements of gas transfer across the free surface, and find a threshold below which mean flow no longer contributes significantly to the gas transfer velocity.

1. Introduction

Turbulent transport is a complex and nonlinear process with great relevance to a variety of scientific and engineering questions. However, the means of generating

[†] Present address: Department of Civil and Environmental Engineering, University of California, Berkeley, Berkeley, CA 94720, USA.

turbulence in a laboratory are limited, most devices falling short of the desired properties of homogeneity, isotropy, and high Reynolds number. Here we introduce a new apparatus that improves the performance of one class of turbulence device – the stirred tank. We do so by employing forcing elements that are randomized in space and time, via a randomly actuated synthetic jet array (RASJA). This is inspired by the success of random forcing in turbulent wind tunnels (Makita 1991; Mydlarski & Warhaft 1996). The apparatus that we describe in this paper has more spatial and temporal degrees of freedom than either these wind tunnels or the prototype randomly stirred tank reported in Variano, Bodenschatz & Cowen (2004). These additional degrees of freedom allow a more thorough exploration of the relationship between random forcing and turbulence. Thus, in addition to demonstrating and characterizing this novel and useful apparatus, we wish to answer two fundamental questions about randomly forced turbulent flow: how sensitive is the flow to the details of the random forcing scheme, and how does one separate the direct effects of random forcing from the turbulence this forcing creates? Answers to these questions will aid in evaluating the growing number of randomly forced devices, and help to ensure that researchers are truly studying turbulence, and not the signatures left by the turbulence generation scheme. After addressing these questions, we use our novel device to study several other questions of fluid mechanical importance: the dynamics of turbulence interacting with a free surface, the spectral form of Eulerian velocity time series, and the amount by which previous measurements of turbulent diffusion may have been affected by tank-specific flows.

Stirred tanks create turbulent flows by shearing the fluid in a manner that does not employ a mean flow. The most common example is the grid-stirred tank (GST) in which a planar grid oscillates in the grid-normal direction through an otherwise unforced fluid. A key advantage of creating turbulence with low mean flow is to reduce the role that advection plays in both mixing and transport. Doing so can enhance mixing rates and allow turbulence to be studied in isolation.

In practice, no device produces turbulence with truly zero mean flow, as some secondary flow is always created as a product of the turbulence generation scheme and/or the interaction of the flow with the boundaries. This small but non-zero mean flow should not be neglected, as it can have strong effects on mixing and transport. For example, we show in §6 that the turbulent flux of gasses across an air–water interface is highly sensitive to mean flow velocity. Thus one should acknowledge and understand the presence of the mean flow in stirred tanks, whether using them to research the physics of turbulence or provide mixing for chemical processes. There is no commonly accepted standard method for calculating mean flow strength in stirred tanks, a topic which we address in §4.2.

We will show in this paper that our new apparatus comfortably out-performs the commonly used GSTs, both in terms of mean flow strength and Reynolds number. However, our apparatus should also be viewed in the context of a different, and complementary, advance in stirred tank technology.

A new generation of stirred tanks has been developed that display homogeneity (and sometimes isotropy) much better than that of GSTs. These symmetric-forcing (SF) systems feature synthetic jets, oscillating grids, or rotating disks arranged symmetrically around some central region (Douady, Couder & Brachet 1991; Villiermaux, Sixou & Gagne 1995; Srdic, Fernando & Montenegro 1996; Shy, Tang & Fann 1997; Voth, Satyanarayan & Bodenschatz 1998; Liu, Katz & Meneveau 1999; Birouk, Sarh & Gökalp 2003; Hwang & Eaton 2004; Webster, Brathwaite & Yen 2004). The symmetric forcing elements drive turbulence which, in the ‘central region’

which is the symmetry point or plane, can be homogeneous and isotropic with low mean flow.

An important advantage of SF systems is that they can, by virtue of their symmetry, create flow that is nearly isotropic at the large turbulent scales (within the central region). This large-scale isotropy fosters small-scale isotropy, and is best achieved by those systems which use eight synthetic jets or fans at the corners of a box to create a three-dimensional isotropic region at the box centre (Hwang & Eaton 2004; Birouk *et al.* 2003, respectively). The large-scale isotropy of a flow is especially important given growing evidence that anisotropy persists in the small scales even at high Reynolds numbers (Pumir & Shraiman 1995; Ouellette *et al.* 2006). This is in contrast to Kolmogorov's prediction of local isotropy at high Reynolds numbers (Kolmogorov 1941, henceforth referred to as K41) and suggests that the large-scale isotropy offered by many SF systems is an important feature when studying the 'canonical' case of turbulence that is isotropic at both large and small scales. A drawback of SF systems is that the flow is optimized only in the limited volume which is the central region. That is, they deliver isotropy at large turbulent scales, but do so for a region smaller than the tank scale. Furthermore, the need for symmetric forcing makes this technique inapplicable to studies of turbulence at boundaries.

In contrast, the RASJA is ideal for studying turbulence at boundaries because it creates turbulence with excellent two-dimensional homogeneity and isotropy, but does so from a single planar source, i.e. without symmetric forcing. Furthermore, the forcing elements of the RASJA cover minimal space, which can be convenient for applications such as creating a turbulent patch in a larger flow. It is important to note, however, that when a single RASJA forces a tank from only one direction, three-dimensional large-scale isotropy is unattainable due to turbulent decay (Maxey 1987). Such asymmetry is by definition unavoidable when studying turbulence at a boundary. When symmetry is not disallowed by the experimental goals, it would be straightforward to combine the RASJA and SF concepts. In fact, the SF system of Hwang & Eaton (2004) includes some random forcing, though with fewer degrees of freedom than the RASJA. By arranging several RASJA arrays in an SF configuration (e.g. several facing planes) one could create a high-Reynolds-number flow with low mean flow and large-scale isotropy extending over a region whose size is limited only by the size of the tank.

The organization of this paper is as follows: in §2 we describe the geometry and construction of the RASJA and the tank which it stirs. In §3, we present the velocity measurement techniques that will be used to evaluate the RASJA's performance. In §4, we consider the random forcing pattern of the RASJA that yields the optimal turbulent flow in our apparatus, and describe the resulting velocity statistics, including the interaction of turbulence with an air–water interface. In §5 we explore the relationship between random forcing patterns and the flow they create. Sections 6 and 7 describe two measurements of fluid mechanics phenomena for which the RASJA is ideally suited. In §6 we measure the effect of secondary flow strength on measurements of the gas transfer velocity across an air–water interface. In §7 we study the form of the Eulerian frequency spectrum, and measure the unknown constant in Tennekes' (1975) model of the inertial-advective range.

2. Apparatus

The stirred turbulence tank is shown in figures 1 and 2. The RASJA sits at the bottom of a rectangular glass tank that is 80 cm by 80 cm wide and 100 cm high. The

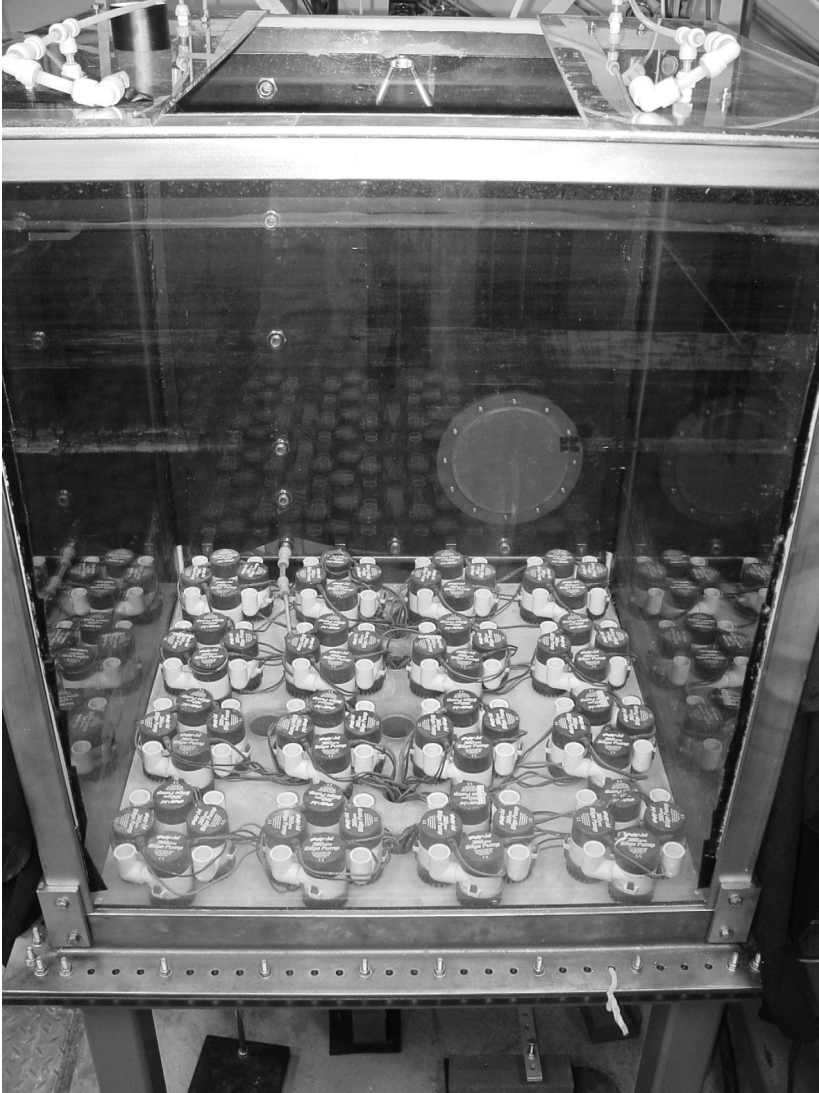


FIGURE 1. The randomly actuated synthetic jet array (RASJA) at the bottom of the tank in which it drives turbulence. The tank width is 80 cm, with 10 cm spacing between the jet nozzles (white cylinders on tank floor).

tank is typically filled to 91.5 cm with water, and the free surface defines $z = 0$. The RASJA is an array of 64 jets arranged in an 8 by 8 grid on the tank floor. The grid has a spacing of 10 cm and obeys reflective symmetry, which was found by Fernando & DeSilva (1993) to reduce secondary flows in GSTs. The jets can be pointed upwards or sideways, though performance is better when upward pointing (see § 5.5). Each jet, when turned on, has a constant exit velocity $U_j = 60 \text{ cm s}^{-1}$ through a cylindrical nozzle of diameter 2.19 cm, giving a jet Reynolds number of 14000. We do not vary the tank Reynolds number by changing the jet Reynolds number but rather by changing the parameters of the spatiotemporal jet driving pattern or the vertical location of the test section.

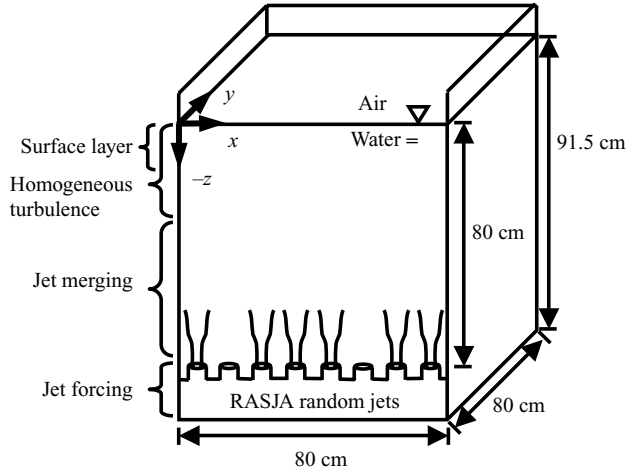


FIGURE 2. Schematic of the stirred turbulence tank, driven by the RASJA at the base.

Each jet is driven by a submerged centrifugal pump, and supplied by fluid through the pump's intake 7 cm beneath the jet nozzle. This intake represents a suction source nearly collocated with the jet, and of equal strength. Because the suction and the jet are always turned on simultaneously, there is zero net mass flux through a control volume surrounding a pump, making each jet a synthetic jet.

Coordinate axes are such that gravity acts in the $-z$ -direction. The tank is symmetric in every (x, y) -plane, and fundamentally asymmetric in the z -direction. Our z -axis is equivalent to what is typically labelled x in wind-tunnel turbulence studies. The synthetic jet nozzles lie in the (x, y) -plane at depth $z = -z_c$ with respect to the free surface at $z = 0$. In the GST literature, z_c is called the “cover”. The jet intakes are 7 cm beneath the jet nozzles, and the tank floor is 4.5 cm beneath that. Typically $z_c = 80$ cm, chosen to achieve symmetry with the tank width and breadth. To preserve this symmetry, we avoid flow disturbances by keeping all plumbing and fittings in the region below the jet nozzles, i.e. $z < -80$ cm. The height of any point above the RASJA itself is defined as $Z \equiv z + z_c$. Elsewhere in this paper, the coordinate system is referred to with indicial notation, i.e. $x_1 = x$, $x_2 = y$, and $x_3 = z$. Velocity components are defined such that U is aligned with x , V is aligned with y , and W is aligned with, but opposite in direction to, z . That is, positive W is upward flow. Velocities are also referred to with indices, such that $U_1 = U$, $U_2 = V$, and $U_3 = W$.

Each synthetic jet can be turned on independently from the others, always at $U_J = 60 \text{ cm s}^{-1}$. The pumps driving each of the synthetic jets are Rule 360 g.p.h. (0.381 s^{-1}) 12 V DC bilge pumps. Flow rates can be altered by limiting the operating voltage, but deviations from the intended 12 V operation create increased wear on the pump motor brushes and shorten pump life. Under normal operation we expect 12000 hours of tank operation before pumps must be replaced.

Pumps are controlled by solid-state relays which are triggered by TTL signals from a Measurement Computing 96 channel digital output card (PCI-DIO96H), controlled by MATLAB at an output frequency of 10 Hz. Each relay, when triggered, closes a circuit supplying 12 V at 2.4 A to a specific pump. If all 64 pumps are turned on simultaneously, the power supply must be able to provide 154 A at 12 V. However, our optimal spatiotemporal jet driving pattern (see §4) uses only a fraction of the pumps at a given time; thus this facility could be operated with a much smaller power supply.

Our relay system is a custom design and fabrication, though a commercially available equivalent is Measurement Computing SSR-RACK48/DST plus SSR-4-ODC-05.

3. Measurement techniques

We characterize the performance of the RASJA based on large-scale and small-scale (one- and two-point, respectively) velocity statistics. Velocities reported herein are measured by acoustic Doppler velocimetry (ADV) or particle image velocimetry (PIV) methods which have complementary strengths. We compare measurements from PIV and ADV whenever possible, and find they give statistically identical results for all comparable quantities. Additional verification of key statistics was performed with a laser Doppler velocimeter (LDV). Results from ADV and LDV confirm that V behaves exactly as U to within statistical uncertainty, as expected from symmetry. Thus the following analysis focuses on the U and W velocity components.

3.1. Statistical methods

We decompose the velocity field $\mathbf{U}(\mathbf{x}, t)$ into its temporal mean $\overline{\mathbf{U}}(\mathbf{x})$ and the fluctuations about this mean, $\mathbf{u}'(\mathbf{x}, t)$. Here, an overbar denotes the time-average linear operator, and boldface type indicates vector quantities. If the velocity field is statistically stationary, then the time-average velocity field $\overline{\mathbf{U}}(\mathbf{x})$ is a good estimator of the expectation value of velocity, $\langle \mathbf{U}(\mathbf{x}) \rangle$. We quantify the magnitude of turbulent velocity fluctuations as $\mathbf{u}_{rms}(\mathbf{x}) \equiv \sqrt{\langle (\mathbf{u}'(\mathbf{x}))^2 \rangle}$.

Statistics reported here are calculated from velocity data subsampled at 1 Hz to ensure independence of samples. The one exception is Eulerian frequency spectra, which utilize high-frequency ADV time series.

Confidence intervals (CIs) are computed directly from individual data records using the Bayesian bootstrap method (Efron & Tibshirani 1993). The half-width of the 95 % CI for quantity a is δa . The CI is also calculated in a frequentist manner, the 95.4 % CI being the region within $\pm 2\sigma$ where σ is the standard deviation of the quantity of interest across an ensemble of independent records. The two CIs are similar, but we prefer to report the bootstrap CI because it represents a more economical use of the data. Additionally, the bootstrap method does not necessitate any assumption about the underlying probability density function of the data.

We verify the repeatability of reported statistics by checking whether independent velocity records measured under identical experimental conditions give values that are identical to within the 95 % CI. In addition to repeatability, we would also like our statistics to be converged. Statistics are converged when they are based on long enough data records to accurately represent the flow properties. Repeatability is a necessary condition for convergence. We quantify statistical convergence for quantity a with a non-dimensionalized measurement uncertainty $a/\delta a$. We consider our measurement of a to be converged when $\delta a/a \leq 0.05$. When repeatability and statistical convergence have been satisfied, doubling the record length will not yield a statistically significant difference in the result.

3.2. Measurements by acoustic Doppler velocimetry

Single-point measurements are made with a Nortek Vectrino ADV (with optional 'plus' firmware). The sample volume is cylindrical, with diameter 6 mm and height 9.1 mm, inside which the spatial average velocity is recorded at a 50 Hz data rate. This data rate corresponds to averaging velocity measurements (obtained at an internal sample rate of 1754 Hz) over a 20 ms interval. For comparison, the smallest scales of turbulence, computed from the dissipation rate ϵ reported in §4.5 and the kinematic

viscosity ν , are the Kolmogorov time scale $\tau_\eta \equiv (\nu/\epsilon)^{1/2} \approx 44$ ms and the Kolmogorov length scale $\eta \equiv (\nu^3/\epsilon)^{1/4} \approx 0.2$ mm.

By virtue of probe geometry, ADV measurements show enhanced precision in the axial direction (\hat{z} in the ADV coordinate system) compared to the radial directions (\hat{x} and \hat{y}). Furthermore, the ADV both disrupts and induces flows (Snyder & Castro 1999). Because of these effects, we collect data with two different ADV orientations. When measuring properties of W , we align \hat{z} (ADV coordinates) with the $-z$ -direction (tank coordinates). When measuring properties of U , we align \hat{z} with the $-x$ -direction.

3.3. Measurements by particle image velocimetry

Digital image pairs for PIV are collected by illuminating passive tracer particles with a laser light sheet. Images are recorded with Uniq Vision 12-bit full-frame-transfer CCD cameras (UP-680CL-12B), with a 494×659 array of $9.9 \mu\text{m} \times 9.9 \mu\text{m}$ pixels, minimum frame transfer time $< 60 \mu\text{s}$ and a maximum frame rate of 60 Hz at full resolution. Illumination is via a two-channel frequency-doubled YAG laser (Spectra Physics PIV 300-10). Each channel's flashlamp and Q-switch, plus the delay between the firing of channel one and two (Δt), are controlled by a digital delay generator (BNC 500A). Laser and camera timing are synchronized with signals controlled in MATLAB via a National Instruments analog output card (PCI-6711).

Tracer particles are hollow glass spheres (Potters Industries Spherical #110P8) with a mean diameter (D_p) of 11 microns and median specific gravity (S) of 1.1. Particle concentration is < 1 p.p.m., thus the particles do not have an appreciable impact on the fluid properties. These particles passively follow the flow, as indicated by their Stokes number $St \equiv \tau_R/\tau_\eta = 0.0159$, where $\tau_R \equiv (S-1)D_p^2/18\nu$ is the particle response time to acceleration. Because $St \ll 1$, the particles follow the flow essentially passively.

Vector velocities are determined using a dynamic central difference scheme over the image pair separation time Δt which is adjusted to optimize the measurements to the observed velocity range $U \approx [-25, 25] \text{ cm s}^{-1}$. Each velocity is found by normalized cross-correlation of small regions of the image pair (Sveen & Cowen 2004). These small regions are size $N \times N$ pixels and known as subwindows. PIV provides a filtered version of the true velocity field, the filter being a box-type filter with box size equal to the subwindow size.

Image pairs are interrogated for velocity vectors at many points, which are arranged along a grid of mesh spacing $N/2$ (i.e. 50% overlap). Interrogation is performed dynamically in a series of iterations, each with a higher resolution than the previous iteration. That is, each PIV velocity field is used as an estimator for another iteration which uses a smaller subwindow. After each iteration, we identify and remove invalid vectors. These include unconverged vectors, for which the normalized cross-correlation does not give a robust indication of particle displacement, and unphysical vectors, which differ from the local spatial median by more than a dynamically determined threshold (Liao & Cowen 2005; Variano 2007). The total number of invalid vectors is less than 10%, and can be left as data gaps or interpolated (e.g. via Delaunay triangularization). We use interpolation to fill data gaps for all except the final iteration. When performing statistical calculations in this paper, we use the final iteration, and prefer working with data gaps because any interpolation scheme represents a smoothing that may affect the results.

The flow we measure has high levels of shear, which requires additional effort in PIV processing. First, shear requires us to keep Δt small, which means that particle displacements are restricted to a limited number of pixels. As a result, velocity estimation to subpixel accuracy is extremely important for this dataset. For this, we employ the spectral continuous subwindow shifting method of Liao &

Set descriptor	standard	close-up	close-up	close-up	large-area
Resolution	medium	low	medium	high	(via MCPIV) high
Image width (cm in x)	5.0	2.6	2.6	2.6	40
Image height (cm in z)	3.8	1.9	1.9	1.9	11.7
Subwindow width (pixels)	48	48	32	24	16
Subwindow width (cm)	0.365	0.226	0.150	0.113	0.4
Grid spacing (cm)	0.182	0.113	0.075	0.056	0.2
Δt (ms)	6	3	3	3	5

TABLE 1. PIV parameters. Subwindows are square. For comparison, note that the relevant flow scales are integral length scale $L_L = 7.5$ cm, Kolmogorov length scale $\eta = 0.0209$ cm and Kolmogorov time scale $\tau_\eta = 0.044$ s. For the close-up dataset, we show the increasing resolution with successive iterations.

Cowen (2005), as they have shown the method to be one of the most accurate and computationally efficient. Second, in early iterations with large subwindow sizes, shear leads to inhomogeneous flow within the subwindows. The resulting ‘shear error’ is mitigated by artificially expanding the imaged size of tracer particles by applying a blurring filter to the images.

The PIV datasets included in this paper are taken with one of three configurations, the details of which are given in table 1. The standard set is used to measure one-point statistics and velocity profiles, the close-up sets are optimized to measure the dissipation rate, and the large-area set helps visualize the tank-scale flow features and also measure the integral length scales. The large-area set is taken using multiple-camera PIV (MCPIV) to achieve a large spatial coverage without sacrificing resolution. In MCPIV, three cameras simultaneously image adjacent (and slightly overlapping) areas of the laser light sheet. Data are then interpolated onto a master grid, yielding a dataset that is ideal for calculating spatial statistics without appealing to Taylor’s frozen turbulence hypothesis (Variano 2007). An example of the output from our PIV analysis is shown in figure 3.

A notable advantage of PIV is that the two velocity components it resolves have equal noise structure, in contrast to the ADV which has different noise levels in each of the three velocity components. Furthermore, in PIV the velocity components are measured orthogonally so that the noise in each is independent from the other. This results in improved estimates of covariance terms (e.g. the Reynolds shear stresses $\langle u_i u_j \rangle$). The ADV, in contrast, exhibits an anisotropic noise structure, and this noise structure is correlated within the (x, z) - and (y, z) -planes. Thus additional care must be taken in error analysis of ADV data.

4. Performance of optimal jet driving pattern

Here we discuss the performance of the tank under the random jet driving pattern that provides the best homogeneity and lowest mean flow (additional details about this pattern are presented in §5.4.2 and figure 12). In this as well as other drive patterns, measurements throughout the tank reveal three large-scale flow regions. With increasing distance from the RASJA, these are the jet-merging region, the homogeneous region, and the surface-influenced region (see figure 2).

From $z = -80$ to $z = -20$ cm is the jet-merging region, in which the direct effects of each jet are noticeable, and thus statistical quantities vary in x and y . Starting

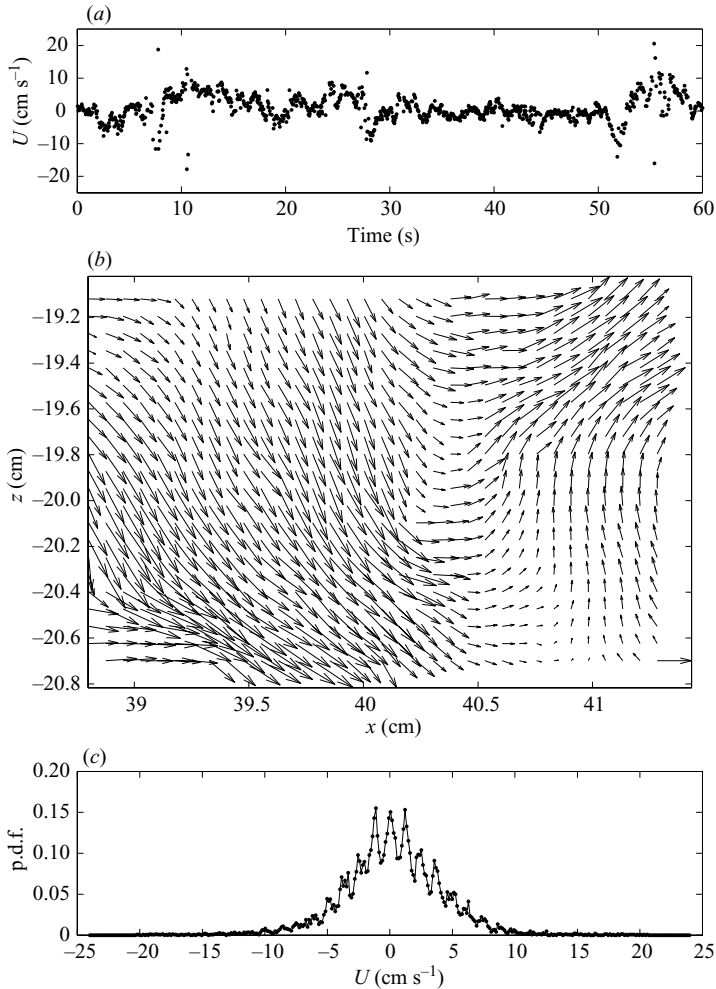


FIGURE 3. Example velocity data from PIV measurements. (a) A subset of the U velocity time series. (b) An instantaneous vector field from the close-up set (medium resolution). For scale, we show a horizontal vector whose length corresponds exactly to 5 cm s^{-1} in the lower right-hand corner of the vector field. (c) The probability density function of the U velocity. The success of the subpixel fitting scheme is evident in the small size of the periodic ‘peaks’ corresponding to integer pixel displacements.

at $z = -20 \text{ cm}$ (a distance from the RASJA equal to 6 times the spacing between jets) velocity statistics are invariant to rotation or translation in the (x, y) -plane. We call this the homogeneous region, and its extent is limited only by the walls and the free surface. In this region, u_{rms} and w_{rms} decrease monotonically with increasing z . The surface-influenced region begins at $z = -15 \text{ cm}$. In this region, a redistribution of turbulent energy towards the surface-parallel directions leads to significant anisotropy (Hunt & Graham 1978). This surface-influenced region is considered further in §4.9, and in §4.1 to §4.8 we focus on the flow in the homogeneous region, reporting measurements at $z = -20 \text{ cm}$ unless otherwise indicated.

On the free surface, signatures of turbulent motion are seen as upwellings (or ‘splats’) and small surface-attached vortices. Qualitative observations of these features show little evidence of a direct connection between the specific state of the RASJA

Quantity	Value	95 % CI
\bar{U}	0.26 cm s ⁻¹	[0.11 0.42]
\bar{W}	0.10 cm s ⁻¹	[-0.11 0.30]
u_{rms}	3.91 cm s ⁻¹	[3.77 4.05]
w_{rms}	4.98 cm s ⁻¹	[4.79 5.16]
w_{rms}/u_{rms}	1.27	[1.20 1.34]
Skewness (u')	0.00	[-0.06 0.05]
Skewness (w')	1.04	[1.00 1.08]
Kurtosis (u')	3.96	[3.83 4.09]
Kurtosis (w')	4.43	[4.28 4.60]
$M_1 = \bar{U}/u_{rms}$	0.07	[0.03 0.10]
$M_3 = \bar{W}/w_{rms}$	0.02	[-0.02 0.06]
L_L	7.57 cm	[7.43 7.72]
L_T	6.36 cm	[6.22 6.50]
\mathcal{T}	2.11 s	[2.09 2.13]
ϵ	5.20 cm ² s ⁻³	[3.43 6.55]
η	0.021 cm	[0.020 0.023]
Re_T	3250	[3120 3390]
R_i	314	[280 386]

TABLE 2. Flow statistics in the RASJA turbulence tank when jets are driven according to the optimal random firing pattern. Measurements are far from the walls, jet array, and free surface. Integral length scales L_L and L_T , dissipation ϵ , and Reynolds numbers are measured over the horizontal region ($x = [20, 60]$, $y = 40$, $z = -20$ cm). All other values are from point measurements at the representative location ($x = 60$, $y = 40$, $z = -20$ cm). Velocity skewness and kurtosis and integral time scale \mathcal{T} are reported from ADV data, while all other values are reported from PIV measurements.

and the turbulent events on the surface. That is, when a jet fires, its signature cannot be seen on the surface (even if the jet's neighbours are not firing). This observation lends support to our assertion that by the time they reach mid-tank, individual jets have merged with the turbulent field and lost the signature of their creation. This picture of jet merging is further supported by the decomposition in § 5.3.1. Finally, we can further support the idea of jet merging by draining the tank while the RASJA is on. When the cover reaches $z_c \approx 40$ cm the structure of free surface motions changes markedly, and the signature of individual jets firing becomes evident.

The jet firing pattern discussed in this section is one in which eight of the jets are firing on average, each for 3 s on average, but in an asynchronous fashion so that the set of firing jets changes every 0.375 s on average. This pattern is described in more detail in figure 12 and § 5.4.2, in the context of our systematic study of driving patterns. Measurements of the flow created by this pattern are summarized in table 2, with details in the following sections.

4.1. Fluctuating velocities

The RMS fluctuating velocity \mathbf{u}_{rms} , calculated from a velocity time series at a single point, is taken as a measure of the intensity of turbulence. Because this quantity includes variance from all sources, turbulent and otherwise, we must consider that the random tank forcing, in and of itself, may obscure the turbulent signal in \mathbf{u}_{rms} . We confirm that \mathbf{u}_{rms} is an appropriate measure of the turbulent intensity by performing the spectral analysis discussed in § 5.3. Our tests of statistical convergence show that values of \mathbf{u}_{rms} converge to the 5 % level in 20 minutes and to the 1 % level in 9 hours when computed from 1 Hz velocity samples.

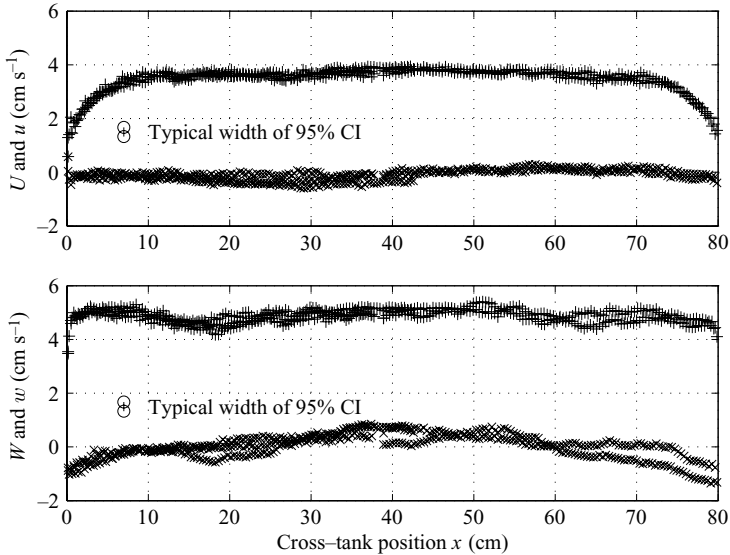


FIGURE 4. Velocity profiles at $z = -20$ cm, + indicates turbulent fluctuating velocities u_{rms} and w_{rms} and \times indicates temporal mean velocities \bar{U} and \bar{W} . The region from $x \approx 15$ to $x \approx 65$ cm shows homogeneity in u_{rms} and w_{rms} . Homogeneity in y can be seen here as well, since the data from $x = 0$ to 40 cm are three overlaid measurements from $y = 30, 35,$ and 40 cm. Data from $x = 40$ to 80 cm are two overlaid measurements, both at $y = 40$ cm. These five measurements, all from different initial conditions, demonstrate the high degree of run to run repeatability. Tank walls at $x = 0$ and $x = 80$ cm induce the mean flow visible in the profile of \bar{W} and cause a departure from homogeneity in the near-wall region.

Examining the horizontal spatial dependence of \mathbf{u}_{rms} , we observe a large region in which it is homogeneous in x and y (to within the 95 % CI). The composite profile of $\mathbf{u}_{rms}(\mathbf{x})$ in figure 4 shows this. The departure from homogeneity in the near-wall region is due to the expected intercomponent transfer of turbulence at a boundary (Hunt & Graham 1978). This wall effect does not extend more than 15 cm ($\approx 2L_L$, see §4.4), therefore leaving a central region of 50 cm which is unaffected by the tank walls.

Anisotropy in the turbulent intensity ($w_{rms}/u_{rms} \neq 1$) is common for tanks without symmetric forcing, and for some SF systems as well (Voth *et al.* 2002). For GSTs, anisotropies are reported in the range $w_{rms}/u_{rms} \in [1.1, 1.4]$ (McDougall 1979; Hopfinger & Toly 1976; DeSilva & Fernando 1994). We measure a value of 1.27 , with a 95 % confidence interval of $[1.20, 1.34]$. Mydlarski & Warhaft (1996) found that active forcing in a wind tunnel increases anisotropy compared to the traditional passive grid wind tunnel, but in our apparatus we see no such anisotropy increase relative to GSTs, despite the RASJA's active forcing.

According to K41 theory, this anisotropy should not be present at smaller scales if the Reynolds number is sufficiently high. However, recent evidence questions this prediction (Pumir & Shraiman 1995; Ouellette *et al.* 2006). Our measurements of small-scale statistics, specifically the structure functions (defined in §4.5), can neither confirm or rule out the presence of small-scale isotropy. Transverse and longitudinal structure functions, calculated in the inertial and dissipation subranges, agree to within statistical uncertainty, but the CIs are large enough to obscure any

anisotropy less than ≈ 1.4 . For example, in the inertial subrange $D_{LL}/r^{2/3} \in [5, 7]$ and $D_{NN}/r^{2/3} \in [6, 8.5] \text{ cm}^{4/3} \text{ s}^{-2}$.

4.2. Mean velocities

A repeatable non-zero mean flow exists in this facility, as evidenced by the horizontal structure in \bar{U} seen in figure 4. The most notable feature is an upward flow near the tank centre and a return flow at the walls. We expect that this is caused by viscous drag at the tank walls. Because the probability distribution of W exhibits positive skewness, upward velocities will be larger on average than downward velocities, and thus will generate a stronger drag force than downward velocities, making the wall regions relatively more attractive for downflow.

To compare the strength of mean flow in the RASJA to that of other stirred tanks, we use the ratio $\mathbf{M} \equiv \bar{\mathbf{U}}/u_{rms}$. Several considerations are important when comparing \mathbf{M} across facilities. First, most GSTs reported in the literature show that \mathbf{M} is largest in the asymmetric direction (e.g. M_3 in our apparatus), thus the performance of a facility may be misjudged by examining only one velocity component (Variano *et al.* 2004). Second, continuity implies that a non-zero mean flow at location \mathbf{x} must be balanced by a mean return flow elsewhere in the tank. As a result, the tank-averaged mean flow will always be zero. Thus if $\bar{\mathbf{U}}(\mathbf{x})$ is averaged over space, the result will tend to zero, resulting in overly optimistic values of \mathbf{M} . For example, spatiotemporal averaging applied to our data from $x = 40$ to $x = 80$ cm would give $M_1 = 0.00$. Thus one must take care to avoid spatial averaging, or do so using non-negative quantities. Herein we use \mathbf{M} as a single-point quantity, which we calculate at many locations before reporting a representative value.

When collecting values of \mathbf{M} from other facilities reported in the literature, we do not have the luxury of raw data, so we must infer values from those statistics which are reported. When ratios are reported directly, some may have been calculated in the overly optimistic ways discussed above. The literature survey by Variano *et al.* (2004) finds values of \mathbf{M} for GSTs which are typically about 0.25 with a best case value of 0.10 in a single coordinate direction. In the worst cases, M_i can exceed 1. We ascribe this poor performance to the tendency of GSTs to drift out of alignment and the deterministic driving pattern that allows mean flows to persist once established. Most symmetric forcing systems perform better than GSTs, with $M_i \approx 0.10$, though if specific attention is not paid to minimizing M_i , symmetric forcing can still yield large mean flows (Liu *et al.* 1999; Webster *et al.* 2004). The facility of Hwang & Eaton (2004) gives the best values in any study to date, with $M_1 = 0.02$ and $M_2 = 0.10$ (note that their apparatus shows symmetry in all three coordinate directions). In our apparatus, \mathbf{M} is quite low, as seen in table 2, namely $M_2 \approx M_1 = 0.07$ and $M_3 = 0.02$. It is encouraging that we find \mathbf{M} to be smallest in the asymmetric direction, which is the opposite of the trend noted above. In §6, we consider the question of how small a mean flow must be before it can be considered negligible.

A different method of quantifying mean flow strength, well-suited for studies of transport processes, is a comparison of the mean flow kinetic energy ($\frac{1}{2}\bar{\mathbf{U}} \cdot \bar{\mathbf{U}}$) to the average turbulent kinetic energy $q^2 \equiv (\frac{1}{2}\bar{\mathbf{u}' \cdot \mathbf{u}'}) = \frac{1}{2}(u_{rms}^2 + v_{rms}^2 + w_{rms}^2)$. This ratio should be calculated everywhere in the region relevant to transport, and then averaged over this region. An approximation to this value can be obtained from PIV data by assuming symmetry in the (x, y) -plane: $M^* \equiv (2\bar{U}^2 + \bar{W}^2)/(2u_{rms}^2 + w_{rms}^2)$. Calculating this and averaging over the representative region $x \in [40, 80]$, $y = 40$, $z \in [-20, -15]$ cm, we find $M^* = 0.0105$.

We find that the mean velocity converges to the 5% level in 25 minutes when computed from 1 Hz velocity samples. Such an average includes many samples of the highly variable temporary mean flows that are intentionally driven by the jet firing pattern, which have a time scale of roughly 0.375 s.

4.3. Higher-order statistics

Higher-order moments of the fluctuating velocity time series at a point ($\mathbf{u}'(\mathbf{x}, t)$) reveal the transport and intermittency properties of the turbulent flow. Compared to the mean and standard deviation, these moments take longer to reach statistical convergence; the highest moment we compute is the kurtosis, which requires 6 hours to converge to the 5% level when computed from 1 Hz velocity samples. The most notable result from these statistics, seen in table 2, is the positive skewness of W , indicating that large upward velocities are more common than large downward ones. This is an expected feature of spatially decaying turbulence, being a signature of the turbulent flux of turbulent kinetic energy (Maxey 1987). A similar skewness is observed in wind-tunnel grid turbulence and increases with Reynolds number (Mydlarski & Warhaft 1996).

4.4. Integral scales

The integral length scale $L_{ij,k}$ is the integral of the spatial autocorrelation function $a_{ij,k}(r)$. This is the normalized autocovariance of velocity time series at two points (u'_i and u'_j) which are separated by a distance r aligned with the coordinate direction x_k . The autocorrelation function is computed from our PIV data as:

$$a_{ij,k}(r) = \frac{u'_i(x_c - \frac{1}{2}r_k) u'_j(x_c + \frac{1}{2}r_k)}{(u'_i(x_c - \frac{1}{2}r_k))^2 u'_j(x_c + \frac{1}{2}r_k)^2}^{1/2} \quad (4.1)$$

for each $r \in [0, \mathcal{L}]$, where \mathcal{L} is the spatial extent of the measurement. Following from this,

$$L_{ij,k} \equiv \int_0^{\mathcal{L}} a_{ij,k}(r) dr.$$

For simplicity of notation we define $L = L_L \equiv L_{11,1}$ and $a(r) \equiv a_{11,1}(r)$. To accurately resolve $a(r)$ and L one must measure over a region $\mathcal{L} \gg L$. If \mathcal{L} is not large enough to include the largest motions, then the resulting calculation of L will be biased. Unfortunately, there is a lack of theory to help us predict the necessary \mathcal{L} and correct any bias caused by using too small an \mathcal{L} . This is because the nature of low-wavenumber (energy-containing) turbulent motions is still poorly understood (Davidson 2004). Such a bias is easily avoided when Taylor's frozen turbulence hypothesis allows time series measured at a single point to be translated into spatially distributed velocity samples. In such cases, one can extend the spatial extent of the velocity record simply by measuring for a longer time period. Taylor's hypothesis does not hold in tanks with low mean flow, thus spatial measurements must be captured directly by PIV or by a probe that rapidly traverses the tank (Thompson & Turner 1975; Brumley & Jirka 1987). We employ the former method, and ensure that L is fully resolved by an examination of the autocorrelation curve. We expect that at large separation r , the autocorrelation curve $a(r)$ will be consistently zero. If a flat region of $a(r) = 0$ is observed as $r \rightarrow \mathcal{L}$, our measurement region is deemed sufficiently large to resolve L . We observe such a region, as shown in figure 5, but note that this is only barely achieved, despite the fact that we measure quite a large area ($\mathcal{L} = 40$ cm). This

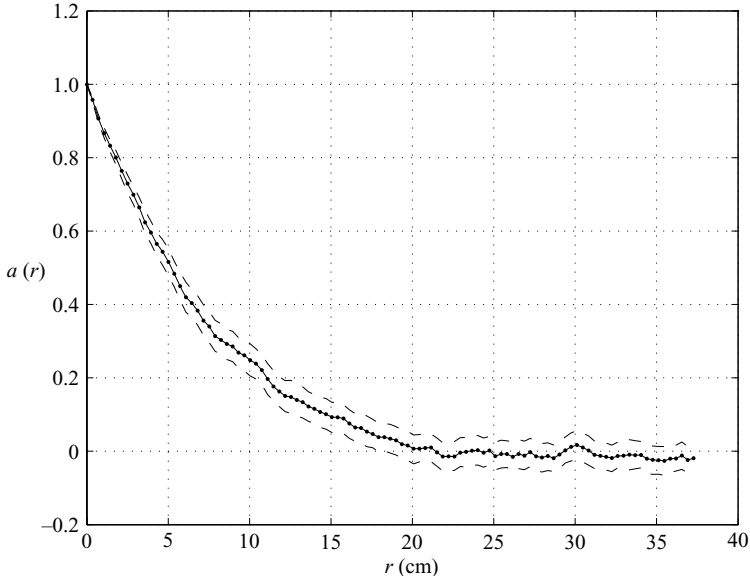


FIGURE 5. Spatial autocorrelation function of horizontal fluctuating velocity, bounded by the 95 % confidence interval (dashed lines). The separation vector r is aligned with x and centred on $x = 40, y = 40, z = -20$ cm. Zero values of $a(r)$ for large r indicates that the measurement area exceeds the average size of turbulent motions.

has two implications. First, it emphasizes that accurate calculations of integral length scales require a large measurement region ($\mathcal{L} > \approx 3L$), which in turn demands a large homogeneous region. Second, it highlights the need when \mathcal{L} is small to calculate $a(r)$ as described in equation (4.1) above. This is because the more common method of obtaining the autocorrelation from the Fourier transform of each velocity subrecord (with cyclic assumption) can give wildly inaccurate results when subrecords are too short.

We compute the integral length scales $L_L \equiv L_{11,1} = 7.57$ and $L_T \equiv L_{33,1} = 6.36$ cm. The 95 % CI bounds shown in table 2 are computed via bootstrap from integrals of replicants of $a(r)$. As with the velocity variance, velocity autocorrelations converge to the 95 % level within 25 minutes, and thus $a(r)$ does as well.

The theory of three-dimensional homogeneous and isotropic turbulence predicts $L_L/L_T = 2$, assuming isotropy of both the small scales and the energy-containing motions (Pope 2000). In our flow, in which the latter assumption does not apply, we measure $L_L/L_T = 1.19$ with a 95 % CI of [1.16, 1.22]. In a related measurement we calculate the integral length scales $L_L^* \equiv L_{33,3}$ and $L_T^* \equiv L_{11,3}$ in which the separation vector r is aligned with the anisotropic flow direction (z). These length scales are more comparable to those measured in wind-tunnel studies using a single probe and Taylor's hypothesis. Here we find $L_L^*/L_T^* = 2.14$ with a 95 % CI of [1.86, 2.43]. The fact that the ratios L_L/L_T and L_L^*/L_T^* bound the predicted value, but fall on opposite sides, is probably due to the anisotropy and inhomogeneity in this flow.

Integral time scales are computed similarly to the length scales, giving $\mathcal{T} = 2.11$ s with a CI of [2.09, 2.13]. Examination of the temporal autocorrelation curve shows that correlations become zero by roughly $5\mathcal{T}$, similar to our result of $3L$ for spatial autocorrelation.

Method	ϵ (cm ² s ⁻³)	95 % CI	95 % CI
Structure function fit	5.20	3.43	6.55
Spectral fit	4.11	3.25	7.41
Scaling law	10	N/A	N/A

TABLE 3. Dissipation rate from three methods. The third method is expected to give the result to within an $O(1)$ constant.

4.5. Dissipation rate

We measure the dissipation rate of turbulent kinetic energy in three ways: scaling law, spectral fit, and structure function fit. While each method includes some assumptions about the flow properties, the results from the three agree quite well, as seen in table 3. A fourth method, the direct calculation from the definition $\epsilon \equiv 2\nu \langle S_{ij} S_{ij} \rangle$, in which the gradients in $S_{ij} \equiv \frac{1}{2}(\partial u'_i / \partial x_j + \partial u'_j / \partial x_i)$ are calculated directly from PIV velocity fields, was also attempted. While this method is quite promising, our initial efforts revealed complications that require further consideration. Specifically, as we refine the PIV resolution so that central differences accurately represent the true velocity gradients, the signal to noise ratio of velocity differences becomes prohibitively small. Because dissipation is a quantity of central importance in turbulence, and PIV a growing technique, further research on sidestepping these problems would be useful. Some promising ideas are using coupled PIV–PTV (Cowen & Monismith 1997), employing a Smagorinsky model to predict subgrid processes (Hwang & Eaton 2004), or resolving unambiguously the larger scales of the dissipation range and fitting to a model dissipation-range spectrum.

Our measurement of the dissipation rate ϵ begins with the order-of-magnitude estimate $\epsilon = A(2/3q^2)^{3/2}/L_L$. Taking A to be 1, we find $\epsilon = 10 \text{ cm}^2 \text{ s}^{-3}$. Comparison with other values in table 3 indicates that in this flow, A is probably closer to 0.5, in agreement with the results of Pearson, Krogstad & van de Water (2002).

Our preferred method of calculating ϵ is based on the structure function in the inertial subrange. Structure functions can be accurately resolved by PIV in a straightforward manner, despite the limited spatial extent and data gaps that present difficulties when calculating quantities in wavenumber space. The second-order longitudinal structure function is defined as

$$D_{LL}(\mathbf{x}_c, \mathbf{r}) \equiv \langle (U_i(\mathbf{x}_c - \mathbf{r}/2) - U_i(\mathbf{x}_c + \mathbf{r}/2))^2 \rangle, \quad (4.2)$$

where \mathbf{r} is aligned with the velocity component U_i . The structure function for $\mathbf{x}_c = \{x = 40, y = 40, z = -20\}$ cm is shown in figure 6, compensated to give ϵ assuming the scaling proposed in K41. That is, for high-Reynolds-number turbulence, in the inertial subrange, K41 predicts $D_{LL} = C_2(\epsilon r)^{2/3}$. Our data agree with this prediction, as shown by the presence of a plateau in figure 6, from which we compute $\epsilon = 5.20 \text{ cm}^2 \text{ s}^{-3}$ with a 95 % CI of [3.43, 6.55]. The confidence interval is based on the bootstrap combined with the uncertainty in C_2 , which we take to be in the range [2.0, 2.2] (Pope 2000).

We also determine the dissipation rate from the one-dimensional velocity power spectrum. According to K41, the power spectrum $E(\kappa)$ exhibits a power-law behaviour in the inertial subrange: $E(\kappa) = C\epsilon^{2/3}\kappa^{-5/3}$, where $C \approx 1.5$ is the Kolmogorov constant. The longitudinal one-dimensional power spectrum in the horizontal direction $E_{11}(\kappa_1)$ is expected to follow a similar power law in the inertial subrange, namely

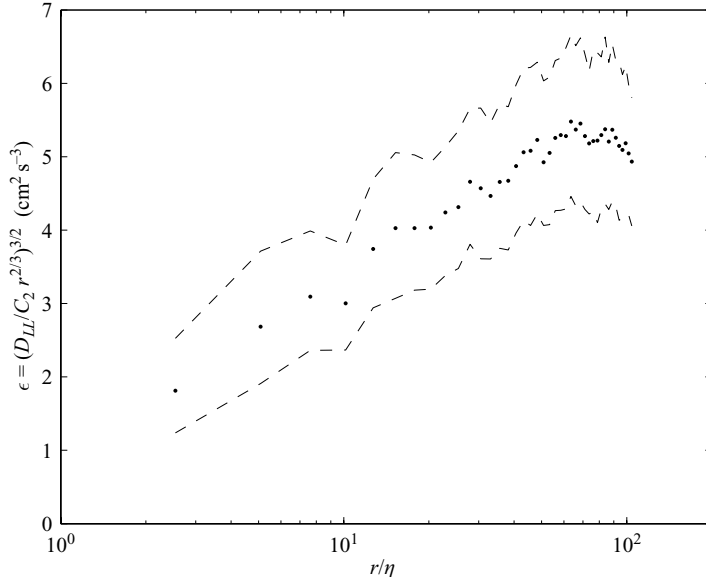


FIGURE 6. Second-order longitudinal velocity structure function, compensated with separation distance r and the constant $C_2 = 2.0$. This is used to calculate the dissipation rate ϵ . Dashed lines give the 95% confidence interval. The Kolmogorov length scale η used to normalize r is determined recursively using the dissipation rate.

$E_{11}(\kappa_1) = C' \epsilon^{2/3} \kappa_1^{-5/3}$ (K41; Pope 2000). This longitudinal one-dimensional spectrum, as computed from our data, is shown in figure 7. It shows a power-law decay range, as well as an exponentially decaying dissipation range; the transition between the two appears near $\kappa_1 \eta \approx 0.1$ as expected from the universal spectrum (Pope 2000). In the inertial subrange, the following equality should be true:

$$E_{11}(\kappa_1) = \frac{C'}{C} E(\kappa), \quad (4.3)$$

in which $C'/C = \frac{1}{2} \frac{18}{55}$, and the $\frac{1}{2}$ arises from our normalization convention (Pope 2000). Using our measured values of L and q^2 as inputs to Pope's model spectrum for $E(\kappa)$, we can determine the value of ϵ that provides the best match between the model and our measurements. Figure 7 shows that our measurements match models in the range $\epsilon = 3$ to $7 \text{ cm}^2 \text{ s}^{-3}$, and a fit to the compensated curve gives $\epsilon = 4.11 \text{ cm}^2 \text{ s}^{-3}$ with a 95% CI of [3.25, 7.41].

We emphasize that particular care must be taken when determining ϵ in this manner, because it is difficult to accurately measure $E_{11}(\kappa_1)$ from discretely sampled data covering a limited spatial region. Turbulent motions that are too large or small to be resolved by the data will be 'aliased' into the subset of resolved wavenumbers. If there is a non-negligible amount of energy in these aliased wavenumbers, then the resolved spectrum will be inaccurate. Thus to accurately measure $E_{11}(\kappa_1)$ and ϵ , velocity records must cover a large spatial extent with fine spatial resolution. The data used here cover 40 cm ($\approx 5.5L$) at 0.4 cm resolution, achieved by the MCPIV technique described in §3.3. We determine that this dataset is capable of providing accurate spectra (i.e. with minimal aliasing) because it accurately resolves the autocorrelation curve as discussed in §4.4.

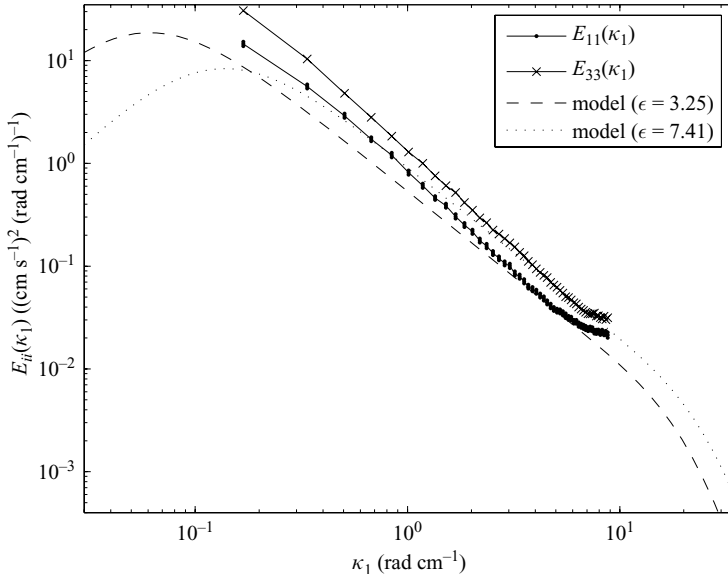


FIGURE 7. Longitudinal (\bullet) and transverse (\times) one-dimensional power spectra at $z = -20$ cm, computed from instantaneous spatial velocity records from $x \in [20, 60]$ cm. The 95 % confidence interval is shown for the longitudinal spectra by additional symbols (\bullet) above and below the curve. The noise floor is evident at the highest wavenumbers. Model spectra, as described in the text, are fitted to different regions of the longitudinal spectrum.

4.6. Reynolds number

Anisotropy in the velocity components leads us to select the following single velocity to be representative of all three components:

$$\mathcal{U} \equiv \sqrt{\frac{2}{3}q^2} = \sqrt{\frac{1}{3}\mathbf{u}' \cdot \mathbf{u}'} = \sqrt{\frac{1}{3}(2u_{rms}^2 + w_{rms}^2)}.$$

From this velocity scale and the dissipation rate, the Taylor-microscale Reynolds number can be calculated as $R_\lambda = \mathcal{U}^2 \sqrt{15/\nu\epsilon}$, where ν is the kinematic viscosity. We find $R_\lambda = 314$ with a 95 % CI of [280, 386]. The turbulence Reynolds number defined by Pope (2000) is $Re_T \equiv \mathcal{U}L/\nu$, where $L = L_L$. We find $Re_T = 3220$ with a 95 % CI of [3100, 3350]. The standard Reynolds number used in GSTs is the grid Reynolds number, Re_G , which is defined in terms of the grid's operating parameters. Hopfinger & Toly (1976) offer a parameterization of \mathcal{U} and L in terms of these operating parameters, with which one can obtain the relationship $Re_G = 2Re_T$. The highest Re_G reported to date is 974, from McKenna & McGillis (2004). We are happy to report that the RASJA provides a much higher Re_G , namely 6440, nearly 7 times as large, and does so with lower mean flow and similar power consumption. This Reynolds number is large enough to justify our use of the predictions of K41 theory used to find dissipation above (Mydlarski & Warhaft 1996).

4.7. Development of steady-state turbulence

While statistical convergence takes minutes to hours, the flow in the RASJA reaches a turbulent steady state rapidly. Instantaneous wavenumber spectra from PIV measurements show a rapid convergence to the ensemble-averaged spectrum when the jets are started from quiescence. If the jets begin firing in the optimal pattern at $t = 0$, instantaneous spectra are statistically identical to each other for all

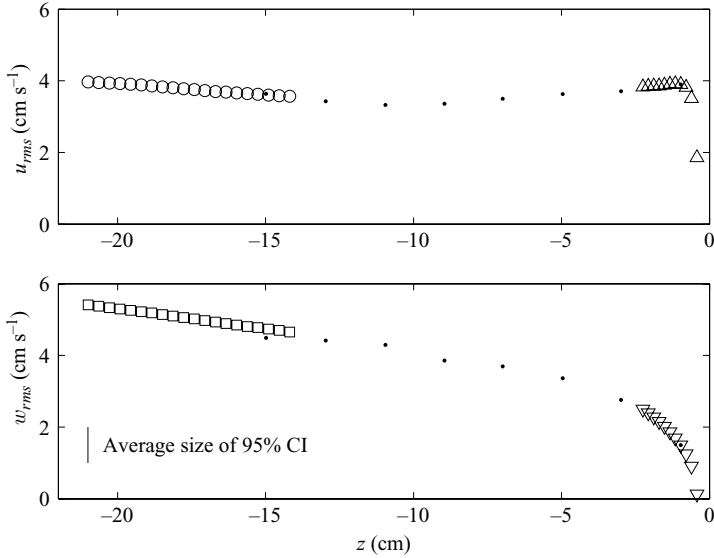


FIGURE 8. Vertical profile of turbulent velocity fluctuation magnitudes beneath the free surface (located at $z = 0$). Evident in this profile is the ‘homogeneous region’ in which turbulent fluctuations decay monotonically, as well as the ‘surface-influenced region’ above $z \approx -12.5$ cm in which energy is transferred between horizontal and vertical fluctuations. Data from the large-area (MCPIV) dataset are shown as \circ and \square . Data from standard-size PIV images are shown as \cdot , in a sparse subset for clarity. Near the surface, the same data are shown in their entirety as \triangle and ∇ . The data shown as \circ and \square are averaged over the horizontal region $x = [20, 60]$ cm and are used to find the power-law decay exponents discussed in §4.8.

times greater than 3 s. The steady state is very repeatable, with mean and RMS values varying by $<5\%$ between measurements taken on successive days. This is in contrast to the GST, in which McDougall (1979) and McKenna & McGillis (2004) find that mean and fluctuating velocities are quite sensitive to initial conditions.

4.8. Vertical profiles of turbulent statistics

The homogeneous region in our tank lies between the jet merging region and the surface-influenced region. The turbulence in this region decays monotonically, as shown in figure 8. The extent of this region is relatively small (i.e. 5 cm) in our apparatus, but could be extended by increasing the distance between the free surface and the jet array. In this region that bears neither the influence of the jet array nor the free surface, we measure the spatial decay of turbulent kinetic energy.

Grid turbulence commonly decays as a power law with distance from the grid, and our data are consistent with this (Pope 2000). We measure the decay with respect to Z , the distance from the RASJA (recall $Z \equiv z + z_c$), and find that $q^2 \sim Z^{-2.30}$, $u_{rms} \sim Z^{-1.01}$, and $w_{rms} \sim Z^{-1.42}$. These results are consistent with GSTs, as reported by Hopfinger & Toly (1976). Far from the grid itself, Hopfinger & Toly obtain $q^2 \sim Z^{-2}$, $u_{rms} \sim Z^{-1}$, and $w_{rms} \sim Z^{-1}$. Closer to the grid, however, they note that w_{rms} decays faster than Z^{-1} , thus q^2 decays faster than Z^{-2} . The decay of q^2 in wind tunnels is more gradual than the decay in either GSTs or the RASJA, being between $Z^{-1.15}$ and $Z^{-1.45}$ (Pope 2000).

The measured decay rate determines whether our apparatus (which is homogeneous in x and y) can be considered homogeneous in z as well. When the spatial decay of q^2 is gradual, the flow can be considered effectively homogeneous in the direction of

decay. Maxey (1987) quantifies this by introducing the decay length scale $L_{decay} = q^2/(dq^2/dx)$ and the effective isotropy criterion $L_L/L_{decay} \ll 1$. The flow in our tank falls short of this criterion: at $Z = 60$ cm (i.e. $z = -20$ cm) we find $L_L/L_{decay} = 0.3$, and the ratio does not drop below 0.1 until $Z = 180$ cm, a height not accessible in our tank. Thus while the RASJA creates turbulence with excellent spatial homogeneity in x and y , there is clear inhomogeneity in z close to the RASJA where turbulent kinetic energy decays rapidly.

The integral length scale remains constant with z in the homogeneous region, to within experimental uncertainty. This may be due to the limited spatial extent of the homogeneous region. Both GSTs and wind tunnels exhibit length scales that grow as the turbulence decays; in GSTs there is some evidence that it grows in such a manner that it exactly balances the decaying q^2 , giving a Re_T that is independent of z . Because we do not find such a balance here, Re_T decays with distance from the source. Thus measurements can be made at a range of Reynolds numbers by changing the location of the test section, as in a wind tunnel.

4.9. Turbulent statistics near the free surface

The effect of the free surface on turbulence is interesting in itself, especially given that the air–water interface is of great importance to engineering and environmental systems. The RASJA allows us to measure these dynamics at a higher Reynolds number than previous studies – our apparatus displays $Re_T = 3250$ compared to $Re_T = 487$ in the experiments of McKenna & McGillis (2004) and $Re_T = 360$ in the large-eddy simulations of Calmet & Magnaudet (2003). The profiles we measure, given in figure 8, show the qualitative features predicted by Hunt & Graham (1978) using rapid distortion theory, namely the redistribution of energy from vertical to horizontal fluctuations. This is expected to occur within one integral length scale of the surface (Calmet & Magnaudet 2003; Hunt & Graham 1978). We observe exactly this, noting that for $z \geq -7.5$ cm, w_{rms} declines more rapidly than its previous (free) decay, and u_{rms} shows a corresponding increase. We also note that some effects are visible at distances up to nearly $2L_L$ ($z = -15$ cm).

Hunt & Graham (1978) predict $w_{rms} \propto -z^{1/3}$ by using inviscid theory. However, in reality there will be a small viscous sublayer, whose thickness Brumley & Jirka (1987) estimate from scaling arguments as $\delta_v \approx 2L_L Re_T^{-1/2}$, using values of L_L and Re_T far from the surface. Calmet & Magnaudet (2003) confirm the accuracy of this estimate, which in our apparatus gives $\delta_v \approx 0.26$ cm. This thickness is slightly smaller than the shallowest depth captured by our PIV measurements, namely $z = -0.42$ cm. Including consideration of the viscous sublayer in the Hunt & Graham prediction yields:

$$w_{rms} = -\beta^{(1/2)}\epsilon^{(1/3)}(z + \delta_v)^{1/3} \quad (4.4)$$

where theory predicts $\beta \approx 1.8$ (Calmet & Magnaudet 2003, citing Hunt 1984 and Magnaudet 2003). Calmet & Magnaudet find that this relation holds between $z \approx -\delta_v$ and $z \approx -0.7L_L$, and measure $\beta \approx 2.0$. We find that this relation holds for depths as great as $z = -1L_L$, and measure $\beta \approx 1.5$.

Nearer to the free surface ($z > -1$ cm) we observe a sudden decay of u_{rms} and therefore q^2 (see figure 9). Comparison with the simulations of Shen, Yue & Triantafyllou (2004, especially their figure 4) indicates that this is probably due to the presence of a surfactant layer on our air–water interface. Such a layer is common in the laboratory unless specific steps are taken to reduce it, and is difficult to eliminate entirely. However, because all natural water bodies have naturally occurring surfactant layers (Frew *et al.* 2004), measurements of turbulence interacting with

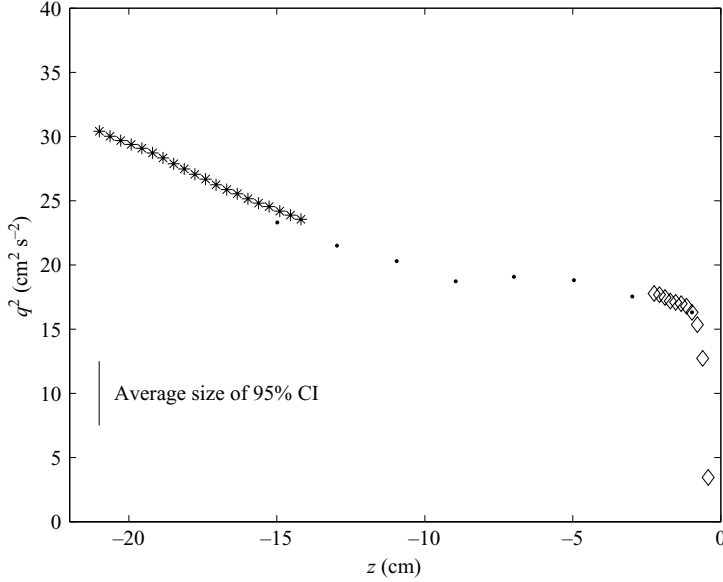


FIGURE 9. Vertical profile of turbulent kinetic energy beneath the free surface (located at $z = 0$). Data are presented in the same manner as figure 8.

a surfactant-covered interface do have direct scientific relevance. The presence of surfactant in our apparatus probably explains the other key difference between our dataset and the behaviour described by Calmet & Magnaudet (2004) and Hunt & Graham (1978). While they report a local minimum in q^2 at $z \approx -L_L/4$, we see no such feature. This can be understood by considering that Shen *et al.* (2004) find a local minimum under a clean free surface at the expected location, but find no such feature when a surfactant is present.

5. Exploration of the jet driving patterns

We explore a variety of jet driving patterns, taking advantage of our high degree of spatial and temporal control. Such an exploration is intended to provide an understanding of which aspects of the random forcing contribute most to creating homogeneous turbulence and why. This should allow future researchers to plan successful variations on our implementation of the RASJA. Importantly, we find that only a small subset of the possible driving patterns provide small mean flow, high Reynolds number, and spatial homogeneity.

Every driving pattern forces the tank through a series of ‘temporary states’. Each temporary state corresponds to a particular set of jets firing, and has an average duration τ_s , which is long compared to the Kolmogorov time scale but short compared to the convergence time over which statistics are calculated. We refer to the flow properties in each temporary state as ‘temporary’ quantities. The performance of each driving pattern is judged based on the following flow properties: mean flow magnitude, free-surface motions, spectral shape, and x, y -planar homogeneity.

The dominant characteristics of a driving pattern are: the number of jets firing at a given instant (§ 5.1); whether the pattern is deterministic or random (§ 5.2); the mean duration for which a jet fires (§ 5.3); and the shape of the distribution of jet

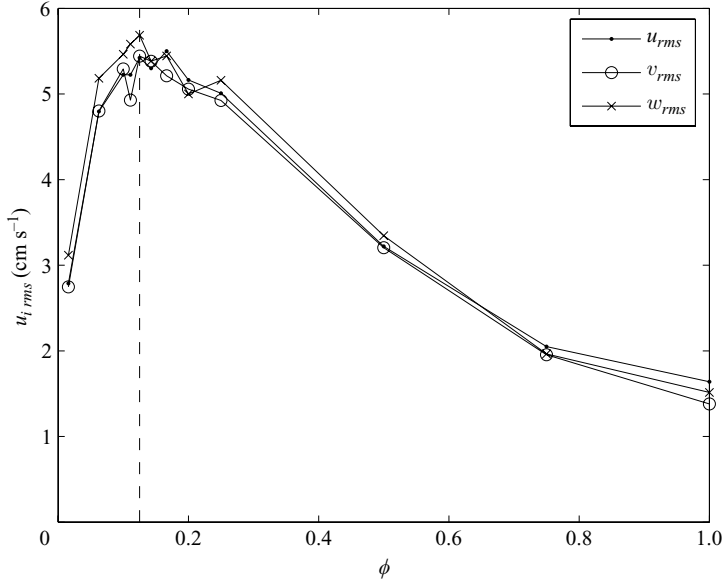


FIGURE 10. The magnitude of turbulent velocity fluctuations as a function of momentum source fraction (the average number of jets which are driving the flow at any instant). There is a peak value near 12.5% (shown by the dashed line) at which the jets insert momentum such that the temporary mean velocity gradients yield maximum turbulent kinetic energy production.

firing durations (§ 5.4). The pattern which we find gives optimal performance is the ‘sunbathing algorithm’ described in § 5.4.2.

5.1. Source and sink fraction

We define the source fraction, denoted ϕ , as the average fraction of jets that are firing at a given time. The related quantity $(1 - \phi)$ is the sink fraction. These are named as such because each firing jet represents a momentum source (upwards from the RASJA into the tank) while each resting jet allows downward momentum flux and thus represents a momentum sink. Considering an analogy to grid turbulence, the source fraction ϕ is similar to the grid porosity and the sink fraction $(1 - \phi)$ is similar to the grid solidity.

When using a grid to create approximately homogeneous and isotropic turbulence, the grid solidity is a key design parameter, for it sets the magnitude and distribution of shear. Similarly, the source fraction of the RASJA has a large impact on the turbulence in our apparatus. We find that there is an optimal source fraction, $\phi_{optimal}$, above which additional momentum input actually reduces turbulent kinetic energy, as shown in figure 10. This behaviour is surprising, in that turning on more jets can actually weaken the turbulence!

We offer an explanation of this surprising behaviour by considering the production of turbulent kinetic energy:

$$P_{ij} = -\langle u_i u_j \rangle \frac{1}{2} \left(\frac{\partial \langle U_i \rangle}{\partial x_j} + \frac{\partial \langle U_j \rangle}{\partial x_i} \right). \quad (5.1)$$

While the mean shear in our apparatus is approximately zero (because $\langle \mathbf{U} \rangle \approx 0$), each temporary tank state has a non-zero mean shear and thus non-zero production.

Drive	M^*	95 % CI	95 % CI
Random, $\phi = 0.25$	0.0215	0.0062	0.0267
Deterministic, $\phi = 0.25$	0.0732	0.0437	0.0864
Random, $\phi = 0.50$	0.1500	0.0618	0.1101
Deterministic, $\phi = 0.50$	0.3738	0.3173	0.4220
Random, $\phi = 0.75$	0.0888	0.0603	0.0758
Deterministic, $\phi = 0.75$	0.3302	0.1997	0.2903
All pumps on, $\phi = 1.00$	0.2358	0.1082	0.1761

TABLE 4. Mean flow energy ratio M^* for random and deterministic drives.

The optimal source fraction is that which maximizes the average magnitude of this temporary mean shear. This implies that for source fractions above $\phi_{optimal}$, the average magnitude of the temporary mean shear decreases with increasing momentum input. In contrast, for source fractions below $\phi_{optimal}$, the average magnitude of the temporary mean shear increases with increasing momentum input.

As seen in figure 10, $\phi_{optimal}$ is very close to 12.5% for random forcing using the sunbathing algorithm (the pattern discussed in §4 and defined in §5.4.2). The fact that $\phi_{optimal}$ exists, and is lower than might be expected *a priori*, could have strong implications for the design of a variety of mixing tanks. Whether the tank is stirred with impellers, synthetic jets, or other mechanisms, more stirring does not necessarily imply better mixing. Rather, additional elements may only add to the strength of the secondary circulation and not to the turbulence itself.

5.2. Random versus deterministic forcing

We wish to understand whether turbulence with low mean flow is better achieved when it is created by a truly random forcing, or whether a deterministic forcing that varies in space and time will perform just as well. To do this, we compare our optimal random driving pattern to a deterministic pattern that mimics it as closely as possible. Both are homogeneous in space on average and have the same mean jet duration ($\mu_{on} = 3$ s, see §5.3).

The results in table 4 show that random forcing consistently achieves a lower mean flow energy ratio M^* than the corresponding deterministic forcings. At lower values of ϕ this is because randomly forced flows have larger q^2 values than flows with deterministic forcing, while at higher values of ϕ this is because random forcing produces weaker mean flows. More details, as well as other supporting experiments, can be found in Variano (2007). Experiments by Mydlarski & Warhaft (1996) in an active-grid wind tunnel support the dominance of random over deterministic forcings. One possible explanation for this is that random forcings include states that ‘frustrate’ any given mean flow pattern, while deterministic forcings will have certain mean flow modes that can be sustained indefinitely.

5.3. Setting the forcing time scale

We now determine the optimal time scale with which to drive the RASJA. This time scale is set by the source fraction (ϕ) and the average duration for which a given jet fires, denoted μ_{on} . These set the average duration of each temporary tank state ($\tau_s \equiv \phi\mu_{on}$), as well as the average time for which a jet remains off ($\mu_{off} = (1/\phi - 1)\mu_{on}$).

Our measurements show that the fluctuating velocity magnitude \mathbf{u}_{rms} increases strongly with μ_{on} . To understand this, we must return to a discussion begun in §4.1.

That is, \mathbf{u}_{rms} measures the variance due to both turbulence and the random tank forcing itself. We must separate these effects before determining the optimal value for μ_{on} .

5.3.1. Separating forced motions from turbulent motions

Consider the decomposition $\mathbf{U} = \overline{\mathbf{U}} + \mathbf{U}_{forced} + \mathbf{U}_{turbulent}$, where the fluctuating velocity $\mathbf{u}' = \mathbf{U}_{forced} + \mathbf{U}_{turbulent}$. The term $\mathbf{U}_{turbulent}$ represents the velocity fluctuations due to turbulence, which is an indirect effect of the tank forcing. The term \mathbf{U}_{forced} represents the temporary mean velocities that are a direct effect of the time-varying tank forcing. These temporary mean velocities are not turbulence, but rather mimic it. This is similar to the thought experiment of an oscillating laminar flow – while such a flow has a non-zero velocity variance, this variance clearly should not be interpreted as a turbulence intensity.

We can determine the relative contributions of $\mathbf{U}_{turbulent}$ and \mathbf{U}_{forced} to \mathbf{u}_{rms} by varying μ_{on} . The separation is subtle, for both components should increase with μ_{on} . The forced fluctuating velocity \mathbf{U}_{forced} should increase with μ_{on} because the duration of each tank state does so as well, allowing each temporary mean flow to become fully developed. The turbulent fluctuating velocity $\mathbf{U}_{turbulent}$ should increase with μ_{on} because more developed mean flows result in a longer-lived mean gradient, allowing more time for the strain and vorticity fields to align for increased turbulent production.

Since both fluctuating components increase with μ_{on} , the key to separating their effects is found in spectral space. We compare the Eulerian frequency spectra of \mathbf{u}' measured over a wide range of μ_{on} values, looking for deviations from the theoretically predicted shape that would indicate velocity fluctuations from sources other than turbulence. Of particular use in this comparison is the limiting case of $\mu_{on} = \infty$ in which a single random tank state remains on for the duration of the measurement, without changing. In this case $\mathbf{U}_{forced} = 0$, i.e. all variance is due to turbulence, though the mean flow will be quite strong. Two such cases are measured, as well as cases with $\mu_{on} = 3, 10, \text{ and } 30$ s.

These spectra, shown in figure 11, show that for smaller values of μ_{on} , (i.e. 3 and 10 s), spectra are identical to the pure turbulent spectra of $\mu_{on} = \infty$. All of these match the shape of the theoretically expected spectra for homogeneous and isotropic turbulence (Tennekes 1975). In contrast, the case of $\mu_{on} = 30$ s shows a broad energy peak at low frequencies (notably lower than $1/\tau_s$). This peak is quite broad, and thus difficult to separate from the low-frequency plateau expected in Eulerian frequency spectra of turbulence. We identify it by the ‘dip’ near $\omega = 0.5 \text{ rad s}^{-1}$ and by the decrease at the lowest frequencies (where we expect a plateau). We hypothesize that this low-frequency peak is the spectral signature of \mathbf{U}_{forced} . This is supported by the observation that when we normalize the $\mu_{on} = 30$ spectrum by any of the others, there is increased energy at low frequencies, but not in the inertial subrange. Thus the amplified low-frequency motions apparently do not contribute to the energy cascade.

This analysis implies that increasing μ_{on} past a certain point does not increase the turbulent production and $\mathbf{U}_{turbulent}$, but rather increases \mathbf{U}_{forced} , the magnitude of the fluctuations directly caused by the tank forcing. This transition appears to be somewhere between $\mu_{on} = 10$ and 30 s. In this paper, to make sure that $\mathbf{U}_{turbulent}$ is dominant, we minimize any possible effect of \mathbf{U}_{forced} by using the smallest μ_{on} available in our tank. If this conservative decision were relaxed, we could achieve larger Reynolds numbers than those reported in §4.6. A practical lower limit for μ_{on} is set by the fact that the pumps driving each jet take ≈ 1 s to reach full flow rate.

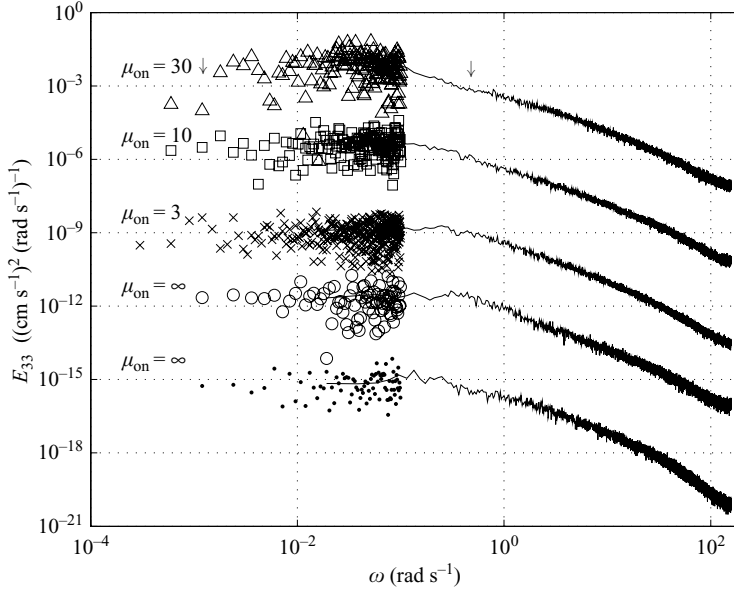


FIGURE 11. Eulerian frequency spectra of w' for five values of μ_{on} . Comparison of these is intended to elucidate what portion of the velocity fluctuations is due to turbulent eddies, and what portion is due to the changing temporary mean flow that varies with the tank state. The spectrum for $\mu_{on} = 30$ s is shown properly normalized (so that its integral from $\omega = -\infty$ to ∞ equals the velocity variance), while all others are shifted downwards by a multiple of 3 decades for ease of comparison. The spectra with $\mu_{on} = \infty$ are driven by two different realizations of a pattern in which synthetic jets are arranged randomly in space and remain steady for all time, thus all variance is due purely to turbulence. Arrows indicate the bounds of the broad, shallow peak in the $\mu_{on} = 30$ spectrum which differs from the shape of these purely turbulent spectra. Each of the five spectra are shown as a composite of two curves, the first shown by symbols and the second by a line. The symbols show the spectrum as calculated from a single long (≥ 90 minute) velocity record, and is shown only for low frequencies. The line is an ensemble average of many spectra obtained by breaking the long record into 5 minute subrecords. The ensemble-averaged curve is less noisy, while the symbols allow insight into the lower frequency components.

We choose $\mu_{on} = 3$ s, which given our value of $\phi_{optimal} = 12.5\%$ yields $\mu_{off} = 21$ s and an average temporary tank state duration of $\tau_s = 0.375$ s.

5.4. Distribution of jet firing durations

Having chosen the mean duration for which jets remain on and off (μ_{on} and μ_{off}), we must now choose the shape of the distributions about these mean values. The distribution of jet firing durations ('on times') is denoted f_{on} , and the distribution of jet resting durations ('off times') is denoted f_{off} . We investigate the cases of Poisson, normal, and constrained normal distributions. The optimal performance is achieved when both f_{on} and f_{off} are normal distributions, which we call the 'sunbathing algorithm'.

5.4.1. Poisson distribution – the 'coin-toss' algorithm

The first distribution used was the simplest one that could give random behaviour and adjustable source fraction. This is a Poisson distribution of jet firing durations, and is obtained via an algorithm which sets each jet's state at every time step. Time steps are separated by $t_u \equiv \mu_{on}/2\phi$, and at each time step, a given jet turns on with

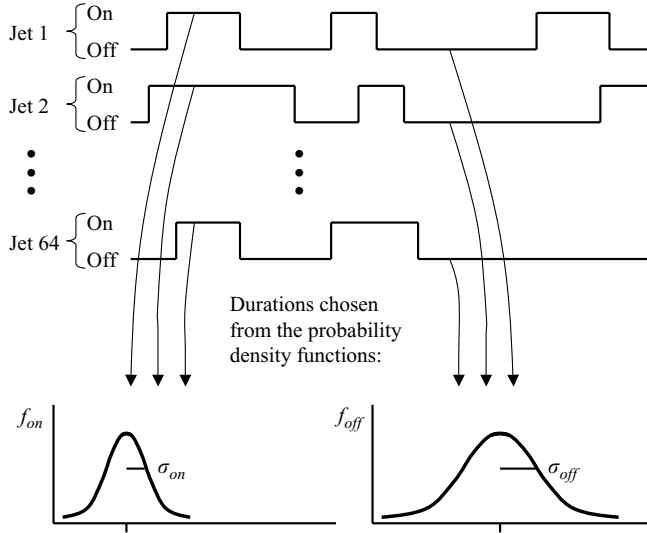


FIGURE 12. Schematic of the ‘sunbathing algorithm’, which is the optimal jet driving pattern. In this, each jet is independent of the others and fires randomly for a duration chosen from the normal distribution f_{on} and then rests for a duration chosen from the normal distribution f_{off} . The flow is quite sensitive to the mean firing duration μ_{on} and the momentum source fraction $\phi = \mu_{on}/\mu_{off}$, but insensitive to σ_{on} and σ_{off} .

probability ϕ . When $\phi = 0.5$ this is equivalent to each jet tossing a coin every time step to determine whether it will be on or off. The width of this distribution is quite narrow and cannot be controlled independently of μ_{on} and ϕ . Performance was poor, showing weak turbulence, high mean flow, and sizable surface waves.

5.4.2. Normal distribution – the ‘sunbathing algorithm’

This is the pattern we have found to be the best, performing well at a wide range of conditions, and constituting the ‘optimal pattern’ for our facility when $\phi = 0.125$ and $\mu_{on} = 3$ s. An example of the pattern is shown schematically in figure 12.

In this algorithm, each time a jet turns on, the jet chooses a duration d_{on} from the normally distributed f_{on} (centred on μ_{on} with variance σ_{on}^2). The jet remains on for this duration, after which it turns off for a duration d_{off} (chosen from the normally distributed f_{off}). After d_{off} has elapsed, the jet turns back on, choosing a new value of d_{on} , and so forth. Each jet independently follows the same procedure, continuously choosing its own d_{on} and d_{off} values from the global distributions f_{on} and f_{off} . We consider the analogy of a sunbather at the beach – after some time in the hot sun, they must go for a swim, after some time cooling off in the ocean they return to sunbathing, etc. Both activities have variable durations, centred on some mean. We use a variety of different initial conditions (i.e. the initial state of each jet) and the flow shows no sensitivity to these. This can be seen in figure 4, in which results from many datasets, each with a different initial condition, are seen to overlap.

We find very little sensitivity of the flow to the values of σ_{on} and σ_{off} . We set $\sigma_{on}/\mu_{on} = \sigma_{off}/\mu_{off} \equiv \sigma^*$ and measure values of $\sigma^* \in \{\frac{1}{6}, \frac{1}{3}, 0\}$. Single-point measurements show that \mathbf{u}_{rms} and \bar{U} are statistically identical at the 95 % confidence level regardless of σ^* at both $\phi = 25$ and 50. Given this insensitivity, we choose to set $\sigma^* = 1/3$. This gives as broad a distribution as possible under the constraint that all

values d_{off} and d_{on} must be positive, noting that if their distributions extend far below zero significant clipping will occur.

It is interesting to note that the case of $\sigma^* = 0$ is equivalent to a discretized delta-function distribution. That is, each pump turns on for exactly μ_{on} and then stays off for exactly μ_{off} . This pattern is more deterministic than the others, in that the relative phases of each pump's sequence are fixed. Despite this additional determinism, tank performance was not significantly affected.

5.4.3. Constrained normal distribution – constant-momentum input

The patterns discussed above allow the number of jets firing at any instant to be different from the average number of jets (64ϕ). Such variability means that instantaneous total momentum input to the tank is not constant. This serves as another manner in which the tank's forcing is randomized. However, to ascertain the effect of this additional randomization, we test an algorithm that provides a constant-momentum input. In this variant of the sunbathing algorithm, the number of jets firing remains fixed. Eight jets are firing initially, and whenever one reaches the end of its chosen duration (chosen from a normally distributed f_{on}), it is replaced by one of the jets that is currently off. Jets remain off until chosen to replace a jet that has just completed its firing duration. The effect of this constraint is to make f_{off} completely dependent on the form of f_{on} .

Under this constant-momentum forcing, tank performance was identical at the 95 % confidence level to the optimal pattern, with respect to homogeneity, q^2 , and M^* . Thus we conclude that variance in the global momentum input does not greatly affect tank performance.

5.5. Jet firing direction

The fact that the jets point upwards may introduce the skewness we observe in W as well as contribute to the anisotropy between W and U, V . Because the former is considered the primary cause for the non-zero mean flow, we attempt to remove this effect by removing any spatial preference in the forcing. We do this by reorienting the jets so that they point sideways. To maintain homogeneity, we orient the sideways jets so that groups of four neighbouring jets collide at one of 16 grid points. This grid obeys reflective symmetry with the tank walls, and we only fire the jets in these groups of four. Thus we have a 4×4 grid of points at which momentum is injected into the flow with minimal directional orientation.

We drive these 16 momentum injection points according to the sunbathing algorithm, with source fractions $\phi \in \{0.125, 0.25, 0.75, 1\}$. These configurations perform poorly compared to upward facing jets, showing nearly twice the skewness, 5–10 times as much mean flow, and about half the u_{rms} (Variano 2007).

6. Effect of mean flow on turbulent scalar transport

Because every turbulent stirred tank has some non-zero mean flow, we wish to determine whether the effects of this mean flow are large enough to demand continued attention. As a case study we investigate turbulent scalar transport, a phenomenon that is commonly studied in stirred tanks. Turbulent scalar transport can be measured in stirred tanks by assuming that advective transport by mean flow is zero. If this is true, then the time rates of change of scalars are due entirely to turbulent diffusive transport. However, if some mean flow is present, we expect that over long time periods even a weak mean flow can overwhelm the effects of turbulent diffusion. This

can be seen by describing scalar transport with the advection–diffusion equation and noting that advective transport scales as t while turbulent diffusive transport scales as $t^{1/2}$. Thus even a weak mean flow can have a non-negligible effect on measurements of turbulent transport.

Conveniently, the spatial control afforded by the RASJA’s forcing elements allows us to separate the effects of mean flow from the effects of turbulent diffusion. We can do this by running a series of transport experiments in which we force mean flows of varying strength by giving jets at certain locations a higher probability of firing. By doing this, we hope to determine the degree to which mean flow may have affected the values currently in the literature. We demonstrate this technique by measuring the bulk O_2 transfer velocity across the air–water interface. Dissolved O_2 is measured with a Clark type sensor (YSI 5331). This probe is located 2 cm beneath the free surface, at $x = 5$, $y = 5$, $z = -2$ cm, and the stirring necessary for accurate readings is simply provided by the RASJA. The tank is initially purged of dissolved oxygen by adding the reagent Na_2SO_3 (0.570 micromolar) and the catalyst $CoCl_2$ (3 micromolar). SO_3 is a strong reductant that reacts with all of the dissolved oxygen in the tank to form SO_4^{-2} . The tank then reaerates from interfacial transfer of atmospheric O_2 (at atmospheric concentration and pressure) across the free surface, and this transfer is enhanced by both the turbulence and the mean flow. The mass transfer velocity k is found by measuring concentration time series ($C(t)$) and fitting for k in the model for flux given by:

$$Flux = \frac{\forall}{A} \frac{dC_{bulk}}{dt} = k\Delta C, \quad (6.1)$$

where A is the tank surface area, \forall is the tank volume, and $\Delta C \equiv C_{surf} - C_{bulk}$. In this last definition, $C_{surf} = C_{sat}$ which is the saturation concentration of dissolved oxygen (determined from Henry’s law) and C_{bulk} is the dissolved oxygen concentration far from the air–water interface.

To vary M systematically, we use spatially dependent source fractions to give the jets near the tank walls a greater likelihood of firing. The 36 inner jets (those not bordering a tank wall) have $\phi_{inner} = 12.5\%$ while the 28 outer jets have $\phi_{outer} \in \{12.5, 25, 50, 75\}\%$. The additional forcing by outer jets produces a tank-scale toroidal mean flow, which for the strongest forcing has a velocity nearly equal to the turbulent fluctuating velocity. For each of these four cases we measure the gas transfer velocity k . The values of k we obtain agree with those reported in McKenna & McGillis (2004), which we extrapolate to our larger Reynolds number. We do this using the ‘dirty’ case from their figure 4, which is appropriate because our free surface is subject to a non-negligible surfactant load.

Our results are shown in figure 13, which demonstrates that there is a 40% increase in k as M^* increases from 0 to 1 (M_1 shows nearly identical behaviour). This increase cannot be attributed to increased turbulent kinetic energy at higher M^* values, because we measure that u_{rms} decreases monotonically (albeit weakly) with increasing M^* . Furthermore, since surfactants impede the gas transfer process, the effect of mean flow on measurements would probably be even stronger under a clean surface.

We conclude that studies currently in the literature probably report values of turbulent diffusivities that are too high. For the case of turbulent interfacial fluxes with a surfactant layer, we expect that values are typically overestimated by 1% to 20% (corresponding to mean flow strengths M_1 between 0.1 and 0.5). The most common value found in the literature is $M_1 \approx 0.25$, which corresponds to a roughly

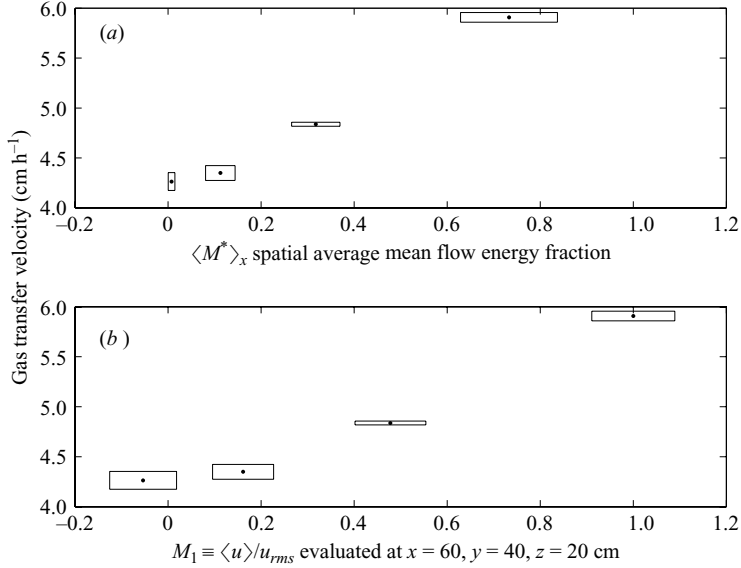


FIGURE 13. Gas transfer velocity k (cm h^{-1}) as a function of the mean flow intensity, showing the sensitivity of transport processes to mean flow in stirred tanks. Two measures of mean flow strength are presented: (a) the spatially averaged energy ratio M^* , averaged over the region $x \in [40, 80]$, $y = 40$, $z \in [-20, -15]$ cm; (b) the single-point single-component ratio of mean to fluctuating velocity, as typically reported in the literature. Boxes show the two-dimensional 95 % confidence intervals.

7 % overestimate of k (Variano *et al.* 2004). The threshold below which mean flow can be considered negligible seems to be $M_1 = M^* = 0.05$, below which the curves k vs. M seem quite flat, and values of k are statistically identical.

7. Eulerian frequency spectrum model

Here we use the turbulent flow generated by the RASJA to contribute to Tennekes' (1975) model of the Eulerian frequency spectrum. This is useful because an improved measurement of model constants would allow researchers to calculate dissipation rates by fitting the model to Eulerian spectra calculated from single-point velocity time series, even when Taylor's frozen turbulence does not hold. This could be especially useful when analysing field measurements of environmental flows.

The RASJA is an excellent tool for studying this model because the mean flow is already absent from measurements (wind-tunnel studies of this model would have to translate measurement devices at the mean flow velocity) and because the high Reynolds number allows a sizable power-law scaling region. Because Tennekes' model is based on homogeneous and isotropic turbulence, an even better apparatus for these measurements would be a tank with symmetric forcing. Nonetheless, the inhomogeneity seen in our apparatus makes our measurements interesting because they more closely resemble the environmental flows where this model may be applied.

Tennekes (1975) performs an analysis of the Eulerian frequency spectrum of velocities in homogeneous isotropic turbulence, and predicts that it should exhibit an inertial-advective subrange of the form

$$E(\omega) = B_0 \epsilon^{2/3} (\sqrt{3} \mathcal{U})^{2/3} \omega^{-5/3}. \quad (7.1)$$

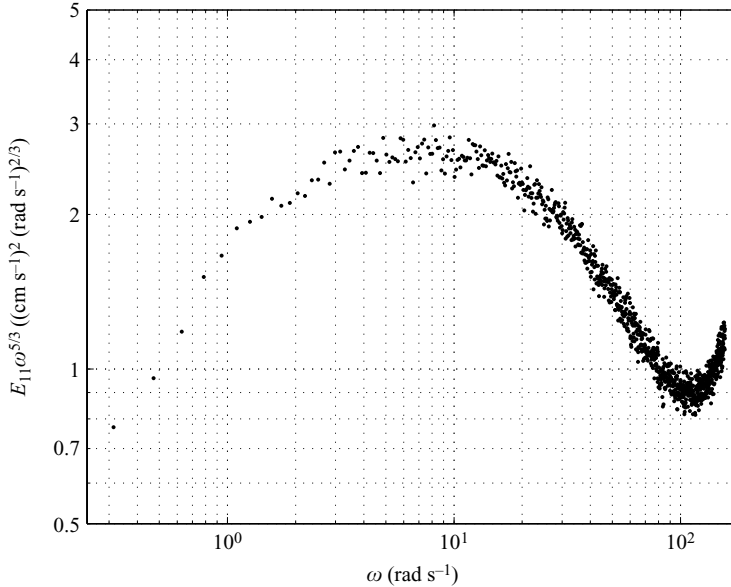


FIGURE 14. Compensated Eulerian frequency spectrum, computed from ADV measurements of the horizontal velocity fluctuation (u') time series (5.5 h of data collected at 50 Hz, ensemble averaged over 40 s subrecords). The flat region represents the inertial–advective subrange from which we can fit to Tennekes’ model, which offers the possibility of calculating dissipation from single-point velocity time series. No data are shown past the Nyquist frequency, rather the upward trend is the noise tail amplified by compensation.

This model includes the effect of small eddies being advected past the Eulerian measurement point by larger eddies, which gives rise to fluctuations of higher frequency than would be observed in a Lagrangian frame. Tennekes suggests that B_0 is of order 1, and Fung *et al.* (1992) calculate 0.8 using further assumptions about the form of the turbulent field. Experimental measurement of this constant is difficult, since it requires a precise measurement of the dissipation rate and an absence of mean flow. Kit, Fernando & Brown (1995) report measurements in a GST at $R_\lambda \in [70, 100]$, confirming the form $E(\omega) = B_1 \epsilon^{2/3} u_{rms}^{2/3} \omega^{-5/3}$ (in which the constant is slightly different, the factor of $\sqrt{3}$ having been absorbed into the constant and only the surface-normal fluctuating velocity used). They report $B_1 \in [0.7, 0.9]$, which is in contrast to earlier work suggesting $B \approx 8$ (DeSilva & Fernando 1994).

The Eulerian frequency spectrum we measure is shown in figure 14 (that for vertical velocity fluctuations is shown in non-compensated form in figure 11). This agrees well with Tennekes’ model, showing the power-law scaling region. Interestingly, the slope of this region appears to be exactly $-5/3$, while the slopes of the wavenumber spectra in figure 7 seem to be slightly steeper than this. From figure 14 we find $B_0 = 0.23$ with a 95 % CI of $[0.16, 0.30]$ and $B_1 = 0.35$ with a 95 % CI of $[0.24, 0.46]$. The uncertainty on this measurement is dominated by the uncertainty in ϵ , for which the percent uncertainty is three times larger than that for $E(\omega)$ and ten times larger than that for u_{rms} . As in §4.5, our normalization of the spectrum assumes the integral over $\omega \in [-\infty, \infty]$ equals the velocity variance.

Our measured value of the constant in Tennekes’ model of the Eulerian frequency spectrum does not resolve the disagreement between previously suggested values. While the constant is apparently non-trivial to measure, we encourage further study

because, if complete, this model could prove to be as useful as Kolmogorov's model of the wavenumber spectrum.

8. Conclusions

No existing device can provide a turbulent flow featuring high-Reynolds-number, large-scale isotropy, and homogeneity over a region much larger than the integral length scale. Facilities providing approximations to this have improved over the past decades, and have proven quite powerful for exploring turbulence, once the limitations of the facilities have been considered. In this study we show that spatiotemporal randomization can greatly improve performance of these systems (whether they employ unidirectional or symmetric forcing) and identify the most important aspects of the random drive pattern.

We find that the flow is quite sensitive to the details of the spatiotemporal forcing pattern. Tank performance is best when forcing is random, and can be greatly improved by setting the average number of firing jets so as to balance the tradeoff between momentum input and turbulent production by local shear. Also important is the time scale of forcing, which should be set to maximize turbulent fluctuations while avoiding fluctuations forced by the random pattern itself. We demonstrate how to monitor this via Eulerian frequency spectra. We find that the shape of the distribution of jet firing durations is a strong driver of tank performance, a normal distribution performing much better than a Poisson distribution. Our measurements show that momentum input need not remain constant for the tank to perform well, and that vertical jets (which insert momentum in the asymmetric direction) give better performance than do horizontally firing colliding jets. These insights should help with both the design of future devices and the interpretation of measurements made in existing randomly forced systems.

Measurements using the RASJA in the optimal configuration show that the flow has a high Reynolds number and is homogeneous and isotropic in planes parallel to the free surface (x, y). The statistical convergence time is long (> 20 minutes for the most basic velocity statistics) but the approach to steady-state turbulence is rapid (≈ 3 seconds). That is, the RASJA develops the desired flow almost instantly, but one must measure this flow for some time to accurately characterize it. We have identified that x, y planar homogeneity is achieved for $Z > 6$ jet spacings (60 cm), after which the velocity fluctuations and Reynolds number undergo a power-law decay with Z . This decay results in a non-zero skewness in W . We find an integral length scale on the order of the jet spacing, and note that boundaries are felt over roughly 2 integral length scales, an important consideration when choosing tank width. We consider one boundary in detail, namely the air–water interface, where we measure its effect on subsurface turbulence at a higher Reynolds number than any previous study. We find good agreement with existing theory and computer simulations.

We have calculated dissipation in three ways, which agree, and support the use of the structure function method as effective and robust. Using this result, we have confirmed the form of the inertial–advective subrange of the Eulerian frequency spectrum predicted by Tennekes (1975) and measured the unknown constant in his model.

Finally, by intentionally forcing mean flows we find there is a statistically significant effect on the measured interfacial gas transfer velocity for mean flows greater than $\approx 5\%$ of the turbulent fluctuating velocity. Many previous studies of gas transfer have been performed in facilities exceeding this threshold. This emphasizes the need to

quantify and report the effects of mean flows in future studies of turbulent transport. We encourage future researchers to use the robust metric of mean flow strength, M^* , presented in §4.2.

The authors gratefully acknowledge the financial support of the National Science Foundation (Grant No. CTS-0093794). Any opinions, findings, and conclusions or recommendations expressed in this material are those of the author(s) and do not necessarily reflect the views of the National Science Foundation. The authors wish to acknowledge the hard work and expertise of Tim Brock, Paul Charles, and Jack Powers in helping to create this facility. Some of the data reported here were captured with the insight and dedicated labor of Seth Schweitzer, James Hunt, and Misty Carlisle. Special thanks goes to Laurent Mydlarski for illuminating discussions during the analyses of tank performance. Finally, the authors would like to thank the editor and three anonymous reviewers for their insights and advice.

REFERENCES

- BIROUK, M., SARH, B. & GÖKALP, I. 2003 An attempt to realize experimental isotropic turbulence at low Reynolds number. *Flow Turb. Combust.* **70**, 325–348.
- BRUMLEY, B. H. & JIRKA, G. H. 1987 Near-surface turbulence in a grid-stirred tank. *J. Fluid Mech.* **183**, 235–263.
- CALMET, I. & MAGNAUDET, J. 2003 Statistical structure of high-Reynolds-number turbulence close to the free surface of an open-channel flow. *J. Fluid Mech.* **474**, 355–378.
- COWEN, E. A. & MONISMITH, S. G. 1997 A hybrid digital particle tracking velocimetry technique. *Exps. Fluids* **22**, 199–211.
- DAVIDSON, P. A. 2004 *Turbulence : An Introduction for Scientists and Engineers*. Oxford University Press.
- DESILVA, I. P. D. & FERNANDO, H. J. S. 1994 Oscillating grids as a source of nearly isotropic turbulence. *Phys Fluids* **6**, 2455–2464.
- DOUADY, S., COUDER, Y. & BRACHET, M. E. 1991 Direct observation of the intermittency of intense vorticity filaments in turbulence. *Phys. Rev. Lett.* **67**, 983–986.
- EFRON, B. & TIBSHIRANI, R. 1993 *An Introduction to the Bootstrap*. Chapman & Hall.
- FERNANDO, H. J. S. & DESILVA, I. P. D. 1993 Note on secondary flows in oscillating-grid, mixing-box experiments. *Phys Fluids A* **5**, 1849–1851.
- FREW, N. M., BOCK, E. J., SCHIMPF, U. *et al.* 2004 Air–sea gas transfer: Its dependence on wind stress, small-scale roughness, and surface films. *J. Geophys. Res.* **109**, C08S17.
- FUNG, J. C. H., HUNT, J. C. R., MALIK, N. A. & PERKINS, R. J. 1992 Kinematic simulation of homogeneous turbulence by unsteady random Fourier modes. *J. Fluid Mech.* **236**, 281–318.
- HOPFINGER, E. & TOLY, J. 1976 Spatially decaying turbulence and its relation to mixing across density interfaces. *J. Fluid Mech.* **78**, 155–175.
- HUNT, J. C. R. & GRAHAM, J. M. R. 1978 Free-stream turbulence near plane boundaries. *J. Fluid Mech.* **84**, 209–235.
- HWANG, W. & EATON, J. 2004 Creating homogeneous and isotropic turbulence without a mean flow. *Exps. Fluids* **36**, 444–454.
- KIT, E., FERNANDO, H. J. S. & BROWN, J. A. 1995 Experimental examination of Eulerian frequency spectra in zero-mean-shear turbulence. *Phys. Fluids* **7**, 1168–1170.
- KOLMOGOROV, A. N. 1941 The local structure of turbulence in incompressible viscous fluid for very large Reynolds numbers. *Dokl. Akad. Nauk SSSR* **30**, 299–303.
- LIAO, Q. & COWEN, E. A. 2005 An efficient anti-aliasing spectral continuous window shifting technique for PIV. *Exps. Fluids* **38**, 197–208.
- LIU, S., KATZ, J., & MENEVEAU, C. 1999 Evolution and modelling of subgrid scales during rapid straining of turbulence. *J. Fluid Mech* **387**, 281–320.
- MAKITA, H. 1991 Realization of a large-scale turbulence field in a small wind-tunnel. *Fluid Dyn. Res.* **8**, 53–64.
- MAXEY, M. R. 1987 The velocity skewness measured in grid turbulence. *Phys. Fluids* **30**, 935–939.

- MCDUGALL, T. J. 1979 Measurements of turbulence in a zero-mean-shear mixed layer. *J. Fluid Mech.* **94**, 409–431.
- MCKENNA, S. P. & MCGILLIS, W. R. 2004 The role of free-surface turbulence and surfactants in air–water gas transfer. *Intl J. Heat Mass Transfer* **47**, 539–553.
- MYDLARSKI, L. & WARHAFT, Z. 1996 On the onset of high Reynolds number grid generated wind tunnel turbulence. *J. Fluid Mech.* **320**, 331–368.
- OUELLETTE, N. T., XU, H., BOURGOIN, M. & BODENSCHATZ, E. 2006 Small-scale anisotropy in Lagrangian turbulence. *New J. Phys.* **8**, 102.
- PEARSON, B. R., KROGSTAD, P. A. & VAN DE WATER, W. 2002 Measurements of the turbulent energy dissipation rate. *Phys. Fluids* **14**, 1288–1290.
- POPE, S. B. 2000 *Turbulent Flows*. Cambridge University Press.
- PUMIR, A. & SHRAIMAN, B. I. 1995 Persistent small scale anisotropy in homogeneous shear flows. *Phys. Rev. Lett.* **75**, 3114–3117.
- SHEN, L., YUE, D. K. P. & TRIANTAFYLLOU, G. S. 2004 Effect of surfactants on free-surface turbulent flows. *J. Fluid Mech.* **506**, 79–115.
- SHY, S. S., TANG, C. Y. & FANN, S. Y. 1997 A nearly isotropic turbulence generated by a pair of vibrating grids. *Expl Therm. Fluid Sci.* **14**, 251–262.
- SNYDER, W. H. & CASTRO, I. P. 1999 Acoustic Doppler velocimeter evaluation in stratified towing tank. *J. Hydraul. Engng* **125**, 595–603.
- SRDIC, A., FERNANDO, H. J. S. & MONTENEGRO, L. 1996 Generation of nearly isotropic turbulence using two oscillating grids. *Exps. Fluids* **20**, 395–397.
- SVEEN, J. K. & COWEN, E. A. 2004 Quantitative imaging techniques and their application to wavy flows. In *PIV and Water Waves* (ed. J. Grue, P. L. Liu & G. K. Pedersen). World Scientific.
- TENNEKES, H. 1975 Eulerian and Lagrangian time microscales in isotropic turbulence. *J. Fluid Mech.* **67**, 561–567.
- THOMPSON, S. M. & TURNER, J. S. 1975 Mixing across an interface due to turbulence generated by an oscillating grid. *J. Fluid Mech.* **67**, 349–368.
- VARIANO, E. A., BODENSCHATZ, E. & COWEN, E. A. 2004 A random synthetic jet array driven turbulence tank. *Exps. Fluids* **37**, 613–615.
- VARIANO, E. A. 2007 Measurements of gas transfer and turbulence at a shear-free turbulent air–water interface. PhD Thesis, Cornell University.
- VOTH, G. A., SATYANARAYAN K. & BODENSCHATZ, E. 1998 Lagrangian acceleration measurements at large Reynolds numbers. *Phys Fluids* **10**, 2268–2280.
- VOTH, G. A., LAPORTA, A., CRAWFORD, A. M., ALEXANDER, J. & BODENSCHATZ, E. 2002 Measurement of particle accelerations in fully developed turbulence. *J. Fluid Mech* **469**, 121–160.
- VILLERMAUX, E., SIXOU, B. & GAGNE, Y. 1995 Intense vortical structures in grid-generated turbulence. *Phys. Fluids* **7**, 2008–2013.
- WEBSTER D. R., BRATHWAITE A. & YEN, J. 2004 A novel laboratory apparatus for simulating isotropic oceanic turbulence at low Reynolds number. *Limnol. Oceanogr.: Methods* **2**, 1–12.